iScience

CellPress
OPEN ACCESS

Article

The *Trypanosoma Brucei* KIFC1 Kinesin Ensures the Fast Antibody Clearance Required for Parasite Infectivity

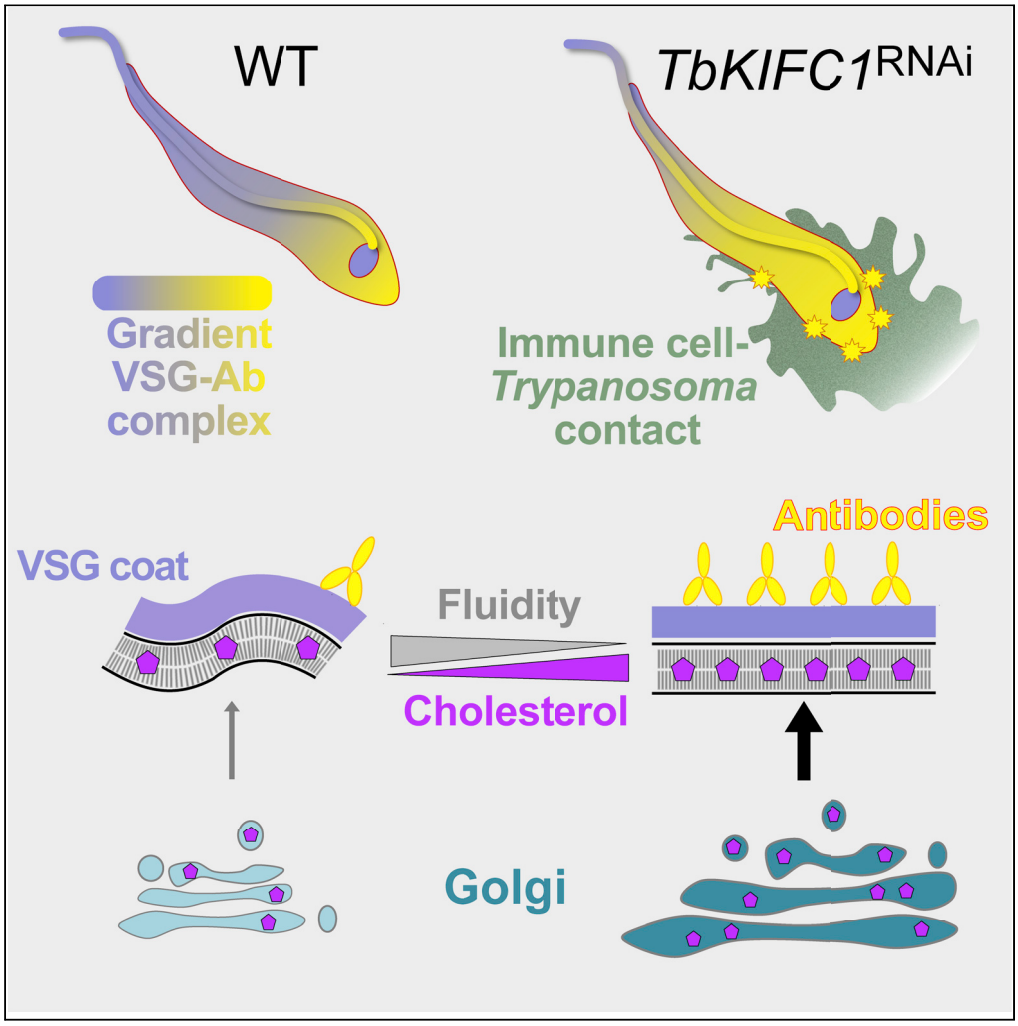

Laurence Lecordier, Sophie Uzureau, Gilles Vanwalleghem, ..., David Pérez-Morga, Derek P. Nolan, Etienne Pays

denolan@tcd.ie (D.P.N.)
epays@ulb.ac.be (E.P.)

HIGHLIGHTS

The *Tb*KIFC1 kinesin preferentially transports cholesterol-containing membranes

*Tb*KIFC1 is absolutely required for parasite growth in mice

Cholesterol trafficking by *Tb*KIFC1 confers high fluidity to the plasma membrane

High membrane fluidity allows antibody clearance necessary for parasite infectivity

Lecordier et al., iScience *23*, 101476
September 25, 2020
https://doi.org/10.1016/j.isci.2020.101476

iScience

CellPress
OPEN ACCESS

Article

The *Trypanosoma Brucei* KIFC1 Kinesin Ensures the Fast Antibody Clearance Required for Parasite Infectivity

Laurence Lecordier,[1] Sophie Uzureau,[1] Gilles Vanwalleghem,[1,9] Magali Deleu,[2] Jean-Marc Crowet,[2] Paul Barry,[3] Barry Moran,[3] Paul Voorheis,[3] Andra-Cristina Dumitru,[4] Yoshiki Yamaryo-Botté,[5] Marc Dieu,[6] Patricia Tebabi,[1] Benoit Vanhollebeke,[7] Laurence Lins,[2] Cyrille Y. Botté,[5] David Alsteens,[4] Yves Dufrêne,[4] David Pérez-Morga,[1,8] Derek P. Nolan,[3,10,*] and Etienne Pays[1,10,11,*]

SUMMARY

Human innate immunity to *Trypanosoma brucei* involves the trypanosome C-terminal kinesin *Tb*KIFC1, which transports internalized trypanolytic factor apolipoprotein L1 (APOL1) within the parasite. We show that *Tb*KIFC1 preferentially associates with cholesterol-containing membranes and is indispensable for mammalian infectivity. Knockdown of *Tb*KIFC1 did not affect trypanosome growth *in vitro* but rendered the parasites unable to infect mice unless antibody synthesis was compromised. Surface clearance of Variant Surface Glycoprotein (VSG)-antibody complexes was far slower in these cells, which were more susceptible to capture by macrophages. This phenotype was not due to defects in VSG expression or trafficking but to decreased VSG mobility in a less fluid, stiffer surface membrane. This change can be attributed to increased cholesterol level in the surface membrane in *Tb*KIFC1 knockdown cells. Clearance of surface-bound antibodies by *T. brucei* is therefore essential for infectivity and depends on high membrane fluidity maintained by the cholesterol-trafficking activity of *Tb*KIFC1.

INTRODUCTION

African trypanosomes (prototype: *T. brucei*) are protozoan parasites able to infect a wide variety of mammals, causing important diseases such as Nagana in bovines and sleeping sickness in humans. The life cycle of these parasites requires developmental forms adapted to the *Glossina* fly vector and mammalian host. In the mammalian bloodstream, trypanosomes are confronted with the host immune response. Bloodstream trypanosomes are entirely covered with a dense monolayer of 10^7 copies of a single type of VSG. Although this dominant antigen triggers an efficient antibody response that clears most parasites, antigenic variation of the VSG ensures that the infection persists long enough for *Glossina* fly-mediated transmission to another host (MacGregor et al., 2012).

In addition to adaptive immunity, primates including humans have developed a specific innate immunity against *T. brucei* (Pays et al., 2014). This immunity results from the trypanolytic activity of the serum protein APOL1, the only secreted member of a family of death-promoting proteins (Hu et al., 2012; Uzureau et al., 2016; Vanhollebeke and Pays, 2006; Wan et al., 2008). The lytic mechanism requires uptake of APOL1, acidic pH-dependent insertion of APOL1 into endosomal membranes, and finally trafficking of these APOL1-containing membranes within the parasite (Pérez-Morga et al., 2005; Vanhamme et al., 2003; Vanwalleghem et al., 2015). APOL1 trafficking to the mitochondrion is a requisite for trypanosome lysis (Vanwalleghem et al., 2015) and involves the kinesin *Tb*KIFC1, which is also associated with the movement of acidocalcisomes (Dutoya et al., 2001; Vanwalleghem et al., 2015). Although *Tb*KIFC1 is more than 1,000-fold more abundant in bloodstream than insect-specific procyclic forms (Dutoya et al., 2001), it is not required for trafficking functions associated with bloodstream forms such as receptor-mediated or fluid phase endocytosis (Vanwalleghem et al., 2015). Moreover, *Tb*KIFC1 down-regulation does not significantly affect parasite growth *in vitro* (Vanwalleghem et al., 2015). Therefore, we investigated the role of this kinesin *in vivo*.

[1]Laboratory of Molecular Parasitology, IBMM, Université Libre de Bruxelles, 12, rue des professeurs Jeener et Brachet, 6041 Gosselies, Belgium

[2]Laboratory of Molecular Biophysics at Interface (LBMI), University of Liège-Gembloux Agro Bio Tech, 2, Passage des Déportés, 5030 Gembloux, Belgium

[3]School of Biochemistry and Immunology, Trinity College Dublin, Dublin 2, Ireland

[4]Louvain Institute of Biomolecular Science and Technology, Catholic University of Louvain, Croix du Sud 4-5, 1348 Louvain-la-Neuve, Belgium

[5]Institute for Advanced Biosciences, CNRS UMR5309, Université Grenoble Alpes, INSERM U1209, 38700 La Tronche, France

[6]MaSUN, Mass Spectrometry Facility, University of Namur, 61 Rue de Bruxelles, 5000 Namur, Belgium

[7]Laboratory of Neurovascular Signaling, Université Libre de Bruxelles, 12, Rue des Profs Jeener et Brachet, 6041 Gosselies, Belgium

[8]Center for Microscopy and Molecular Imaging (CMMI), Université Libre de Bruxelles, 12, Rue des Profs Jeener et Brachet, 6041 Gosselies, Belgium

[9]Present address: School of Biomedical Sciences, The University of Queensland, St Lucia, QLD 4072, Australia

[10]These authors contributed equally

[11]Lead Contact

*Correspondence: denolan@tcd.ie (D.P.N.), epays@ulb.ac.be (E.P.)

https://doi.org/10.1016/j.isci.2020.101476

This work resulted in the unexpected discovery that *Tb*KIFC1 is instrumental not only in human innate immunity against the parasite but conversely it is also essential for parasite evasion of host adaptive immunity.

RESULTS

*Tb*KIFC1 Preferentially Interacts with Cholesterol-Containing Membranes

To understand the function of *Tb*KIFC1, we considered first its membrane-interacting potential. The *Tb*KIFC1 N-terminal region contains a vesicular trafficking VPS27/Hrs/STAM (VHS) domain made of eight helices (H1–H8) (Figure 1A). Homology modeling (Arnold et al., 2006) suggested that this VHS is composed of four double-stranded hairpins (Figure 1B). As measured by incubation with membranes containing various spotted lipids, the recombinant VHS domain exhibited binding to anionic lipids, such as phosphatidylinositols (PI) and phosphatidylserine (PS), but no binding to cholesterol alone (Figure 1C). In Langmuir monolayer adsorption experiments (Nasir et al., 2017), this domain adsorbed faster to dimyristoylphosphatidylserine (DMPS) than dimyristoylphosphatidylcholine (DMPC) (initial velocity [IV] = 0.52 $\pm$ 0.04 and 0.19 $\pm$ 0.00 mN/m/min, respectively), particularly in the presence of cholesterol, which strongly increased VHS binding to the lipids (IV = 1.41 $\pm$ 0.13 mN/m/min) (Figure 1D, upper panel). In these experiments, the surface pressure variation at equilibrium, which reflects the penetration power of the VHS domain into a lipid monolayer, was also the highest in the presence of DMPS + cholesterol (Figure 1D, lower panel). Therefore, *Tb*KIFC1 preferentially interacted with membranes containing anionic lipids and cholesterol. Interestingly, helix H7 of the VHS contains a motif predicted to bind cholesterol (CARC: 116 KRYHTV 121) (Fantini and Barrantes, 2013), which may explain the particular affinity of the *Tb*KIFC1 VHS for cholesterol-containing anionic lipids.

Since the C-terminal helical hairpin H7H8 not only contains a possible motif for cholesterol binding but also exhibits a combination of hydrophobic and positively charged amino acids compatible with lipid binding (Figure 1A), the affinity of this hairpin for lipids was assessed by molecular dynamics and docking approaches. Using a coarse grained representation, a 1-μs simulation of a PC/PS system in the presence of H7H8 showed this hairpin to be located at the phospholipid polar head/acyl chain interface, with residues V103, I107, V111, W114, and Y118 of helix H7 facing the membrane interior (Figure 1B, lower panel; Figure 1E, upper panel). Helix H7 interacted better with PS than PC (Figure 1E, lower panel). Using docking simulation, the relative interaction energy of H7H8 was found to be −80 and −50 kcal/mol for assembly with five PS and five PC molecules, respectively. Langmuir monolayer experiments confirmed that PS favors the insertion of H7H8 into model membranes, since both maximal insertion pressure (MIP) and attractiveness factor ($\Delta\Pi$) of the synthetic H7H8 peptide were increased with PS (Figure 1F). In contrast, a mutant H7H8 peptide termed VHS7, where the hydrophobic residues predicted to contact the membrane were replaced by alanine (V103A/I107A/V111A/W114A/Y118A), had significantly lower MIP and $\Delta\Pi$ values than the wild-type (WT) version (Figure 1F). Accordingly, the mutant VHS7 domain exhibited much slower adsorption to lipids than the WT, and the preferential binding to PS and cholesterol relative to PC was strongly reduced (IV = 0.07 $\pm$ 0.00, 0.10 $\pm$ 0.03 and 0.09 $\pm$ 0.01 mN/m/min for DMPC, DMPC/DMPS, and DMPC/DMPS/cholesterol, respectively) (Figure S1). We conclude that helix H7 allows *Tb*KIFC1 VHS binding to PS- and cholesterol-containing membranes.

*Tb*KIFC1 Transports Endosomal Membranes

The role of *Tb*KIFC1 in membrane trafficking was investigated in trypanosomes expressing the wild-type (WT) kinesin or its mutant VHS7 version. In these experiments, APOL1-mediated killing of *TbKIFC1*^{RNAi} cells was measured following addback of recoded (thus, RNAi-insensitive) versions of the *Tb*KIFC1 gene (Vanwalleghem et al., 2015), either as WT or VHS7 (see Figures 1G and S2, for evidence of *Tb*KIFC1 down-regulation and addback re-expression in the RNAi line). As expected (Vanwalleghem et al., 2015), addback of the recoded WT version restored normal trypanolytic activity following knockdown of the endogenous *Tb*KIFC1 transcript (Figure 1H). However, addback of the recoded VHS7 mutant did not (Figure 1H). This result indicated that the VHS7 mutant, which interacts poorly with membranes, has lost its APOL1 trafficking activity.

Biotin ligase (BL)-conjugated versions of addback *Tb*KIFC1, both WT and VHS7, were employed to identify proteins proximal to the kinesin, following chromatography of cellular extracts on streptavidin (Roux et al., 2012) (see Figures 1G and S2, for evidence of proper expression of BL-conjugated *Tb*KIFC1). As expected, this screen identified several tubulin-related components, in particular two proteins biotinylated by the *Tb*KIFC1-BL conjugate, a tubulin polymerization promoting factor (Tb927.4.2740) and a tubulin-associated

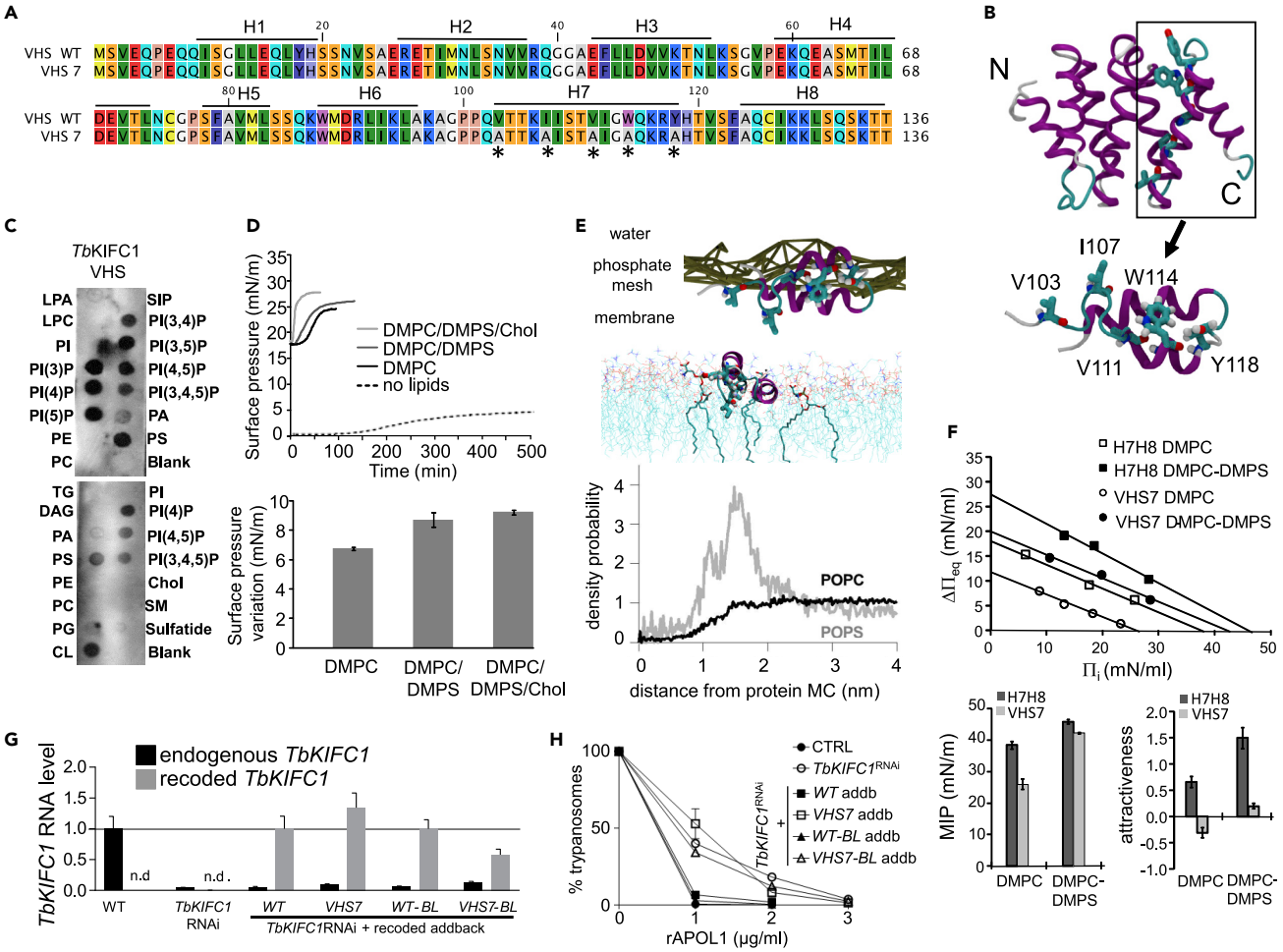

Figure 1. Role of *Tb*KIFC1 in Membrane Trafficking

(A) WT and VHS7 mutant sequences of the *Tb*KIFC1 VHS domain, with indication of the different helices (H1–H8). The asterisks point to the mutations in VHS7.

(B) Model of the VHS domain, built by homology modeling with 1ELK and 1X5B (PDB codes) as templates. The inset shows the H7-H8 helical hairpin (*Tb*KIFC1 H7H8). Lower panel: model of helices H7H8 highlighting residues V103, I107, V111, W114, and Y118, mutagenized into A in VHS7.

(C) Immunodetection of recombinant VHS (0.5 μg/mL) association with various lipids spotted on membrane strips (LPA, lysophosphatidic acid; LPC, lysophosphocholine; PI, phosphatidylinositol; PI(3)P, PI(3)phosphate; PI(4)P, PI(4)phosphate; PI(5)P, PI(5)phosphate; PE, phosphatidylethanolamine; PC, phosphatidylcholine; S1P, sphingosine-1-phosphate; PI(3,4)P2, PI(3,4)bisphosphate; PI(3,5)P2, PI(3,5)bisphosphate; PI(4,5)P2, PI(4,5)bisphosphate; PI(3,4,5)P3, PI(3,4,5)trisphosphate; PA, phosphatidic acid; PS, phosphatidylserine; TG, triglyceride; DAG, diacylglycerol; PG, phosphatidylglycerol; CL, cardiolipin; Chol, cholesterol; SM, sphingomyelin; Blank, no lipid).

(D) Adsorption of recombinant VHS domain into an air-water interface (without lipids) or into a lipid monolayer with DMPC, DMPC-DMPS (1:1), or DMPC-DMPS-cholesterol (1:1:2). Top panel: kinetics; bottom panel: variation of surface pressure at equilibrium. Data are represented as mean ± SD; n = 3.

(E) Molecular dynamics of the interaction between the *Tb*KIFC1 H7H8 peptide and a membrane composed of PC/PS (9:1). In the top section of the figure, the peptide is represented as in (B) (lower panel), and the membrane is represented by a line joining the phosphate groups. The bottom section shows the radial distribution function of POPC (black line) and POPS (red line) around the peptide mass center (MC).

(F) Interaction with PS. The adsorption of the H7H8 helices of *Tb*KIFC1 into a lipid monolayer composed of DMPC with or without DMPS (1:1) was evaluated by measuring maximal insertion pressure (MIP, dark gray bar) and attractiveness factor ($\Delta\Pi$, light gray bar). The WT and VHS7 mutant version of H7H8 (see A) are compared. MIP corresponds to the x-intercept of the linear regression (inset) of $\Delta\Pi_{eq}$ (surface pressure at the equilibrium) versus Π_i (initial pressure). Data are represented as mean ± SD; n = 3.

(G) Relative expression levels of the endogenous or ectopic *TbKIFC1* genes in various *TbKIFC1*^{RNAi} cell lines with or without addback *TbKIFC1*expression (WT or VHS7), as measured by quantitative RT-PCR. Data are represented as mean ± SEM; n = 3. (addb refers to the different recoded *TbKIFC1* addback sequences reinserted in the RNAi line, provided or not with a biotin ligase [BL] tag).

(H) Involvement of H7 in APOL1 transport, as measured by trypanolysis as a function of rAPOL1 concentration during incubation with control (CTRL) or *TbKIFC1*^{RNAi} parasites. Data are represented as mean ± SEM; n = 3.

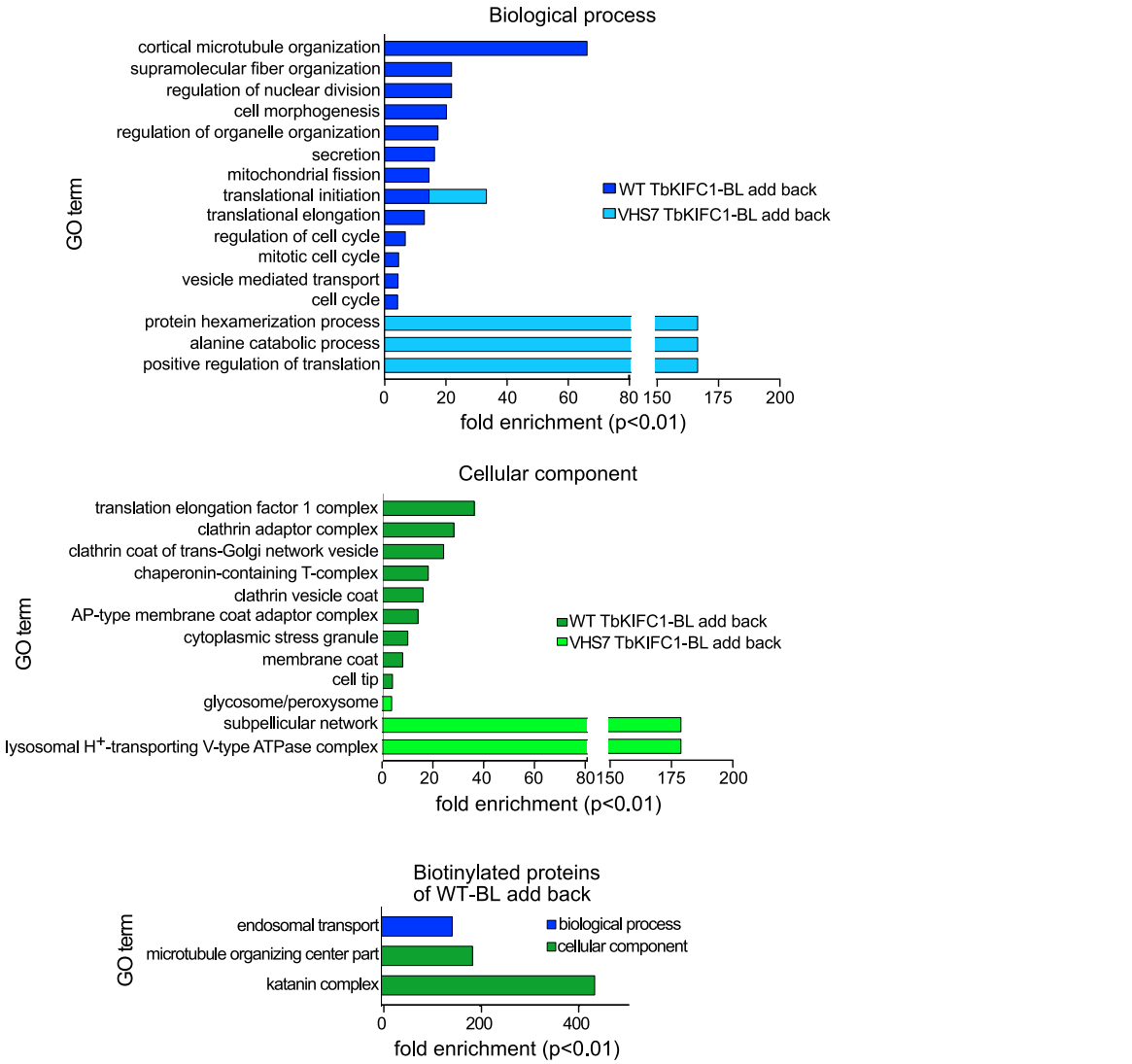

Figure 2. Proteins Associated with *Tb*KIFC1

The proteome associated with BL-conjugated *Tb*KIFC1, either WT or VHS7 mutant, was characterized by mass spectrometry of proteins bound to streptavidin agarose beads. These proteins were analyzed for their relationship with cellular components and biological activity in TriTryp database through Gene Ontology terms enrichment. See Table S1 for the list of identified proteins.

AIR9-like protein (Tb927.11.17000) (Table S1). In addition, the WT *Tb*KIFC1-BL-associated proteome, but not the VHS7 version, included several proteins involved in vesicular membrane traffic, in particular the vacuolar protein sorting-associated protein 4 (VPS4) (Tb927.3.3280) and the katanin p60-like protein 2 (Tb927.10.1210), which contains a VPS4 C-terminal oligomerization domain and is predicted to transport endosomes (https://tritrypdb.org/tritrypdb/app/record/gene/Tb927.10.1210). The p60-like katanin probably contacted *Tb*KIFC1, since this protein was biotinylated by the *Tb*KIFC1-BL conjugate (Table S1). Thus, proteins involved in endosomal traffic were significantly enriched in the fraction isolated from cells expressing BL-conjugated WT *Tb*KIFC1 but not VHS7-BL (Figure 2 and Table S1). We conclude that the H7 helix of *Tb*KIFC1 VHS is involved in both APOL1 and endosomal membrane trafficking.

*Tb*KIFC1 Is Required for Evasion of the Parasite from Adaptive Immunity

Since expression of *Tb*KIFC1 is restricted to bloodstream forms, we considered the possible involvement of this kinesin in functions linked to the VSG and immune evasion. These studies involved generating cloned

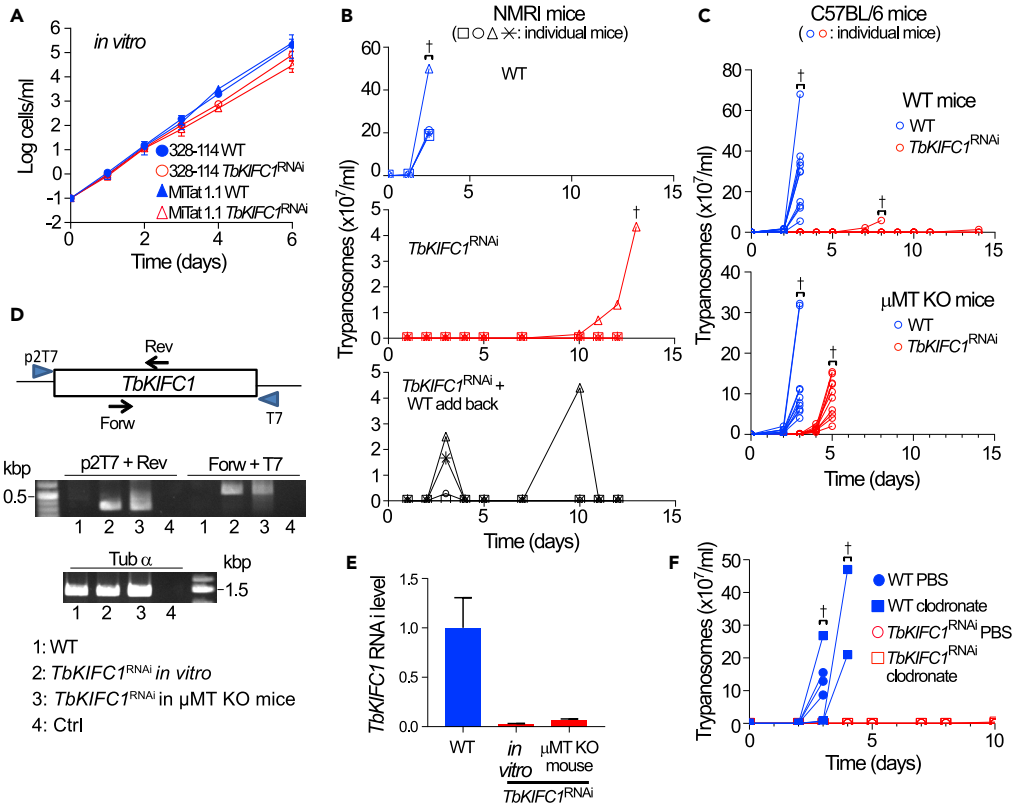

Figure 3. Role of *Tb*KIFC1 in Parasite Growth

(A) Cumulative *in vitro* growth of two independent *T. brucei* lines, either WT or *TbKIFC1*^{RNAi}. Data are represented as mean ± SD; n = 3.

(B) Trypanosome parasitemia in four NMRI mice infected intraperitoneally with 10^5 *T. brucei* 328-114 bloodstream forms (WT), *TbKIFC1*^{RNAi}, or *WT* addback *TbKIFC1*^{RNAi} parasites. The infection was monitored for each individual mouse (n = 5).

(C) Parasitemia in 10 WT or B cell-defective (µM KO) C57BL/6 mice infected intraperitoneally with WT or *TbKIFC1*^{RNAi} parasites. The infection was monitored for each individual mouse (n = 2).

(D) PCR detection of the *TbKIFC1* RNAi construct in the genomic DNA of WT *T. brucei*, or in *TbKIFC1*^{RNAi} trypanosomes grown either *in vitro* or in µM KO mice (day 5) (CTRL = no DNA). Data are represented as mean ± SD; n = 3.

(E) RT-PCR detection of *TbKIFC1* RNA in WT *T. brucei*, or in *TbKIFC1*^{RNAi} trypanosomes grown either *in vitro* or in µM KO mice (day 5). Data are represented as mean ± SD; n = 3.

(F) Parasitemia in three C57BL/6 mice infected intraperitoneally with WT or *TbKIFC1*^{RNAi} parasites after prior injection of liposomes containing either phosphate buffer (PBS) or clodronate. The infection was monitored for each individual mouse (n = 2).

TbKIFC1^{RNAi} cell lines in MiTat 1.1 parasites because of the availability of anti-MiTat 1.1 VSG IgGs, IgMs, and immune serum (O'Beirne et al., 1998). Both the previous (Vanwalleghem et al., 2015) and these new *TbKIFC1*^{RNAi} cell lines exhibited only slightly reduced *in vitro* growth rate relative to WT parasites (Figure 3A). In striking contrast, the *TbKIFC1*^{RNAi} trypanosomes were unable to infect mice, whereas WT parasites killed the animals within 3 days (Figures 3B and 3C). The detection of parasites in one mouse after day 10 was probably due to loss of knockdown of *Tb*KIFC1 in the parasites. Addback of recoded WT *Tb*KIFC1 (Vanwalleghem et al., 2015) into the *TbKIFC1*^{RNAi} trypanosomes partially restored parasite infectivity, as three of four mice infected with these cells developed a parasitemia (Figure 3B). The partial nature of this restoration of infectivity probably reflected the low expression of recoded *Tb*KIFC1 in these cells relative to true WT levels (see Figure 6E in Vanwalleghem et al., 2015). The growth of *TbKIFC1*^{RNAi} cells *in vitro* but not *in vivo* indicated a functional requirement for *Tb*KIFC1 for growth in the mammalian host. Significantly, inoculation of *TbKIFC1*^{RNAi} trypanosomes in B cell-deficient mice (µMT KO) allowed full recovery of infectivity after a delay of 3 days (Figure 3C), despite the fact that parasites growing in these mice still exhibited strong down-regulation of *Tb*KIFC1 linked to the conservation of the RNAi construct in these cells (Figures 3D and 3E). Thus, the infectivity of *TbKIFC1*^{RNAi} cells was compromised because of the

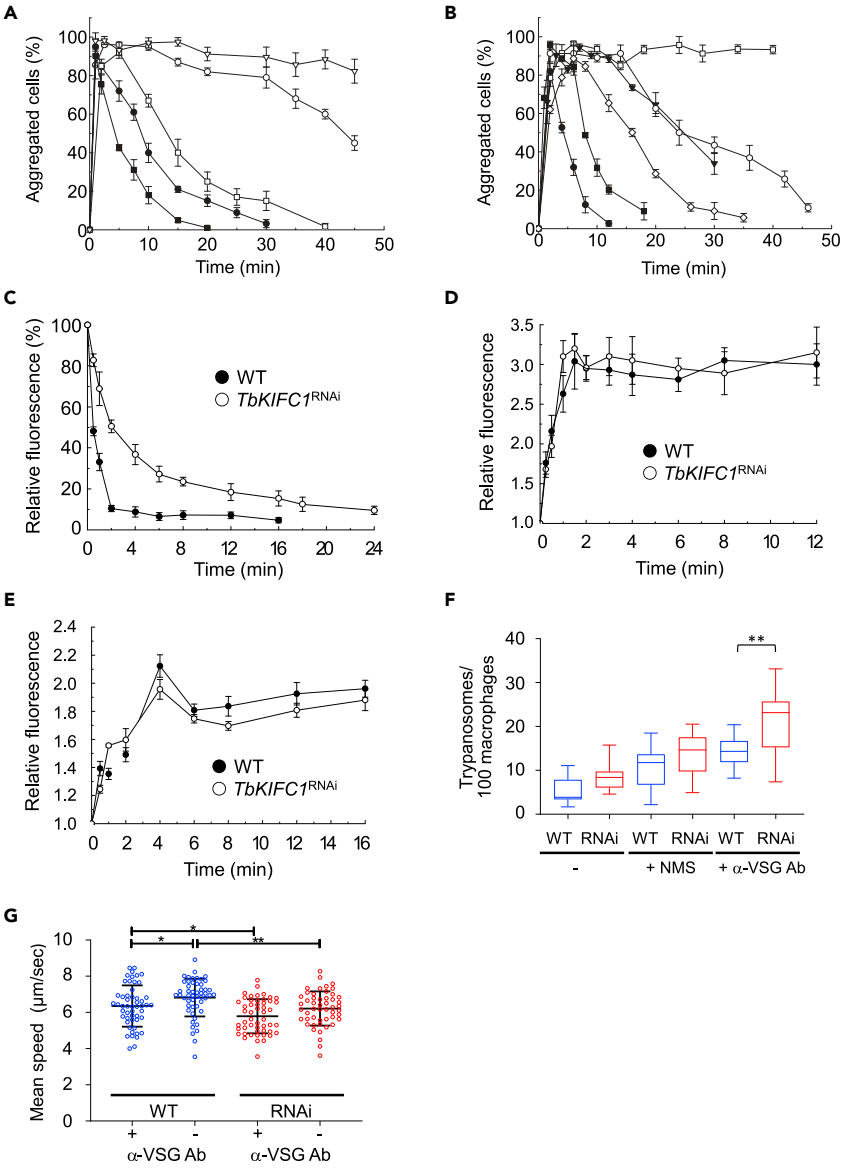

Figure 4. Role of *Tb*KIFC1 in Surface Trafficking of VSG/Antibody Complexes

(A) Disaggregation of WT or clone 1 *TbKIFC1*^{RNAi} cells following addition of anti-VSG IgGs as follows: WT: ■, 1 μg/mL; ●, 2 μg/mL; *TbKIFC1*^{RNAi} cells: □, 1 μg/mL; ○, 2 μg/mL; ▽, 3 μg/mL. Data are represented as mean ± SD; n = 3.

(B) Disaggregation of WT and *TbKIFC1*^{RNAi} cells following addition of purified anti-VSG IgMs as follows: WT: ▼, 40 μg/mL; ■, 16 μg/mL; ●, 8 μg/mL. *TbKIFC1*^{RNAi} cells: □, 16 μg/mL; ○, 8 μg/m; ◇, 4 μg/mL. Data are represented as mean ± SD; n = 3.

(C) Clearance of surface-bound antibodies as determined by flow cytometry of WT and clone 1 *TbKIFC1*^{RNAi} cells incubated with anti-VSG immune serum. The data are expressed as percent median fluorescence intensity detected relative to time zero. Data are represented as mean ± SD; n = 3.

(D) Internalization of surface-biotinylated VSG. After incubation at 37°C for various times, internalization of surface-biotinylated WT in clone 1 *TbKIFC1*^{RNAi} cells was determined by flow cytometry. The data are expressed as percent median fluorescence intensity detected relative to time zero. Data are represented as mean ± SD; n = 3.

(E) Return of internal biotinylated VSG to the surface. After incubation at 37°C for 15 min, membrane traffic of surface-biotinylated WT and *TbKIFC1*^{RNAi} cells (clone 1) was cold-stopped and the remaining surface biotin was removed with reduced glutathione. The appearance of surface biotin was determined by flow cytometry after incubation for various times at 37°C. The data are expressed as in (D). Data are represented as mean ± SD; n = 3.

Figure 4. *Continued*

(F) Binding and uptake of WT and *TbKIFC1*^{RNAi} parasites by murine RAW264.7 macrophages, after parasite incubation or not for 30 min with either 10% normal mouse serum (NMS) or anti-MITat 1.1 VSG antibodies. Data are represented as mean ± SD; n = 3. One-way ANOVA, Sidak's multiple comparison test **p < 0.01.

(G) Mobility of WT and *TbKIFC1*^{RNAi} trypanosomes after incubation or not with anti-MITat 1.1 VSG antibodies. The data are from a representative experiment. Data are represented as mean ± SD; n = 3. ANOVA/Dunn's multiple comparison test *p < 0.01; **p < 0.05

host antibody response, and *Tb*KIFC1 was required to overcome this response. Interestingly, suppression of phagocytic activity was not sufficient to rescue the virulence defect in *TbKIFC1*^{RNAi} cells, as these cells were unable to infect mice treated with clodronate liposomes to deplete mononuclear phagocytes (Figure 3F).

*Tb*KIFC1 Is Required for Clearance of VSG/Antibody Complexes

VSG-antibody complexes are rapidly cleared from the surface of trypanosomes, and it has long been speculated that this clearance might have relevance for parasite survival in the mammalian host (Cheung et al., 2016; Engstler et al., 2007; O'Beirne et al., 1998; Barry, 1979). This clearance has been characterized by monitoring parasite disaggregation after incubation with purified anti-VSG antibodies (O'Beirne et al., 1998). Significantly, disaggregation of trypanosomes treated with anti-VSG IgGs was far slower in *TbKIFC1*^{RNAi} cells (in three independent lines) than in WT cells, and the magnitude of the effect increased with the antibody level (Figures 4A, S3A, and S3B). Since IgM is the first antibody to appear after initial exposure to VSG (O'Beirne et al., 1998) and IgM is cleared more rapidly than IgG (Engstler et al., 2007), the effect of knockdown of *Tb*KIFC1 on clearance of anti-VSG IgM was examined (Figure 4B). In all cases the disaggregation of WT trypanosomes was faster than that of *TbKIFC1*^{RNAi} cells. Moreover, the effect for IgMs appeared to be more pronounced than for IgGs. For example, WT parasites and *TbKIFC1*^{RNAi} parasites treated with IgMs (8 μg/mL) had a $T_{1/2}$ for disaggregation of 5 and 25 min, respectively. At higher levels of IgMs (16 μg/mL), *TbKIFC1*^{RNAi} cells failed to disaggregate during the course of the assay, whereas WT cells disaggregated with a $T_{1/2}$ of 10 min (Figure 4B). However, at lower levels of IgMs (4 μg/mL), clearance of antibody was apparently so fast in WT parasites that no aggregation could be observed (not shown), but aggregation of *TbKIFC1*^{RNAi} cells was obvious (Figure 4B). The same results were obtained with two other *TbKIFC1*^{RNAi} clones (Figure S3C).

A more direct assay of antibody clearance from the surface of individual cells, by flow cytometry, confirmed a substantial reduction in clearance in *TbKIFC1*^{RNAi} cells (Figures 4C, S4A, and S4B). Immunofluorescence microscopy provided visual confirmation of this delay (Figure S4C).

In *VSG*^{RNAi} parasites (Cheung et al., 2016), clearance of anti-VSG antibodies was also compromised owing to the decreased packing density of VSG on the surface. However, there was no obvious difference in the level of VSG expressed in *TbKIFC1*^{RNAi} lines relative to WT cells (Figure S5A). Moreover, the pattern and relative intensity of the labeling of VSG and other proteins after surface biotinylation was essentially identical in *TbKIFC1*^{RNAi} and WT cells (Figure S5B). Finally, there was no significant difference in the internalization of biotinylated VSG in *TbKIFC1*^{RNAi} compared with WT cells (Figure 4D), nor was there a significant difference in the return of internalized biotinylated proteins back to the surface (Figure 4E).

Therefore, knockdown of *Tb*KIFC1 only affected the surface mobility of antibody-VSG complexes but not the expression, surface location, or trafficking of the VSG itself.

*Tb*KIFC1 Influences Both Parasite Capture by Macrophages and Swimming Speed

To evaluate the influence of antibody persistence on the surface in *TbKIFC1*^{RNAi} parasites, trypanosomes were co-incubated with macrophages after opsonization with normal mouse serum (NMS) or anti-VSG antibodies. *TbKIFC1*^{RNAi} parasites exhibited higher antibody-mediated capture by macrophages than WT trypanosomes (Figures 4F and S6A). Knockdown of *Tb*KIFC1 also resulted in a slight reduction in the trypanosome swimming speed (Figure 4G). This effect was not linked to detectable structural changes in the flagellum, such as in the flagellar axoneme and associated structures, paraflagellar rod (PFR), and flagellum associated zone (FAZ) (Figure S6B). There is evidence that motility is essential for infectivity (Shimogawa et al., 2018), so even though the defect in *TbKIFC1*^{RNAi} parasites is very slight, it may explain their increased capture by macrophages even in the absence of specific antibodies (Figure 4F), as well as the slower development of the infection in μMT KO mice (Figure 3C).

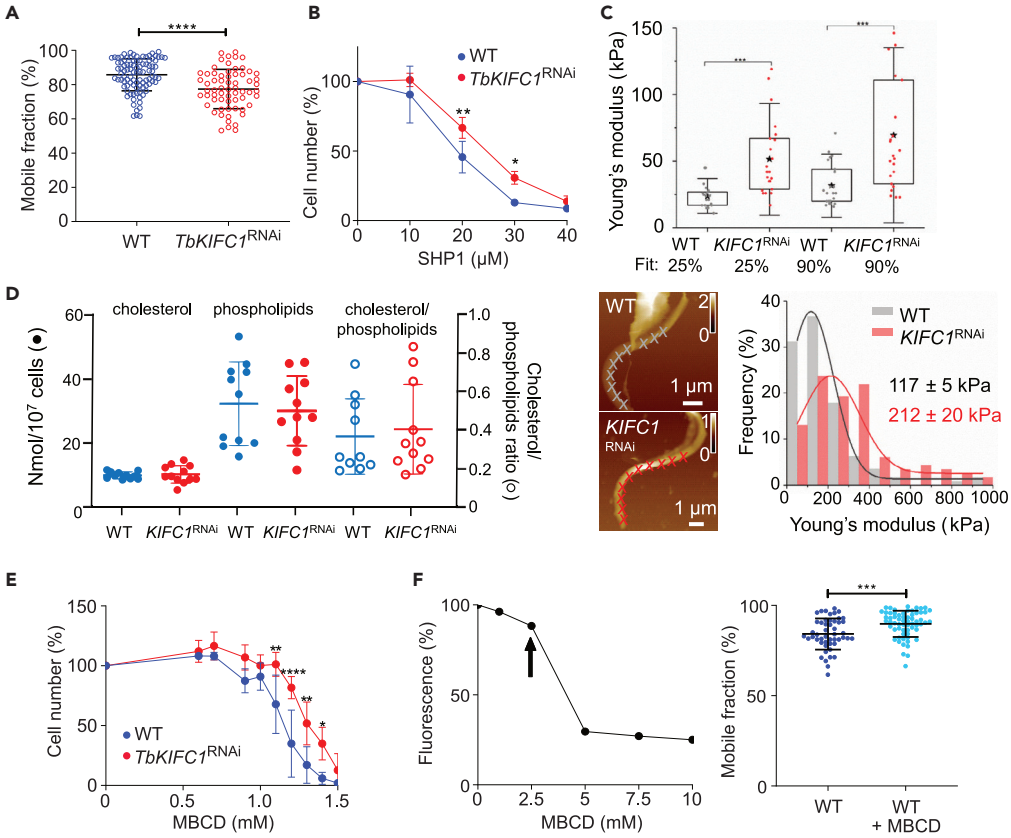

Figure 5. Role of TbKIFC1 in Plasma Membrane Dynamics

(A) VSG mobility in the plasma membrane of WT and *TbKIFC1*^{RNAi} trypanosomes, as measured by FRAP. Data are represented as mean ± SD; n = 3. Mann-Whitney test ****p < 0.0001.

(B) Sensitivity of WT and *TbKIFC1*^{RNAi} trypanosomes to the toxicity of the membrane-stiffening peptide SHP1. Data are represented as mean ± SD; n = 3. Two-way ANOVA, Sidak's multiple comparison test *p < 0.05; **p < 0.01.

(C) Atomic force microscopy (AFM) measurements of trypanosome surface mechanical properties. Upper panel: Young's modulus values of the cellular body membrane of individual WT (gray dots) and *TbKIFC1*^{RNAi} (red dots) trypanosomes assessed from AFM multiparametric imaging. Values were extracted from force curves using Hertz fits up to 25% (mainly plasma membrane contribution) and 90% (mainly microtubules contribution) of the maximum applied force. Bottom left: AFM height images of the flagellum of WT and *TbKIFC1*^{RNAi} trypanosomes. Crosses indicate the location along the flagellum where single force-distance curves were extracted and fitted with the Hertz model to obtain the Young's modulus (scales in μm). Bottom right: histograms and corresponding Gaussian fit revealing the elastic Young's modulus of WT and *TbKIFC1*^{RNAi} flagella. Data are representative of n ≥ 30 cells per condition. Data are represented as mean ± SD; n = 6. One-way ANOVA test ***p < 0.001.

(D) Comparison of cholesterol and phospholipid amounts in WT and *TbKIFC1*^{RNAi} trypanosomes. Data are represented as mean ± SD; n = 3.

(E) Trypanosome resistance to 18-h incubation with increasing amounts of MBCD. Data are represented as mean ± SD; n = 3. Two-way ANOVA, Sidak's multiple comparisons test *p < 0.05; **p < 0.01; ****p < 0.0001.

(F) Effect of MBCD on cholesterol levels and plasma membrane fluidity of WT parasites. Left panel: the MBCD concentration necessary to obtain 10% reduction of cholesterol, as measured by flow cytometry of parasites incubated with Top Fluor cholesterol, was determined to be 2.5 mM (arrow). Right panel: FRAP analysis of WT parasites pre-incubated or not for 30 min with 2.5 mM MBCD. Data are represented as mean ± SD; n = 3. T test ***p < 0.05.

*Tb*KIFC1 Influences Plasma Membrane Fluidity

The effects of *TbKIFC1*^{RNAi} on trypanosome speed and surface mobility of antibody-VSG complexes were consistent with a change in the physical properties of the surface membrane, for example, membrane fluidity. In order to evaluate the relative fluidity of the membrane, the kinetics of membrane fluorescence recovery after photobleaching (FRAP) were measured on *TbKIFC1*^{RNAi} and WT cells. This recovery was slower in *TbKIFC1*^{RNAi} trypanosomes, suggesting that the fluidity of the plasma membrane, and hence VSG mobility, is lower in these cells (Figure 5A). Accordingly, *TbKIFC1*^{RNAi} trypanosomes were more

resistant to the SHP-1 peptide, a membrane stiffening peptide that inserts preferentially into fluid membranes (Harrington et al., 2010) (Figure 5B). Finally, multiparametric atomic force microscopy (Krieg et al., 2019) showed an increase in the rigidity of the *TbKIFC1*^{RNAi} surface, on both the cell body (Figure 5C, upper panel) and the flagellum (Figure 5C, lower panel). In both WT and *TbKIFC1*^{RNAi} cells the flagellar surface was more rigid than the cellular body, most likely due to the higher cholesterol content of the flagellar membrane (Sharma et al., 2017). Taken together, these observations indicated that knockdown of *Tb*KIFC1 results in a less fluid and more rigid plasma membrane.

*Tb*KIFC1 Reduces the Cholesterol Level of the Plasma Membrane

Cholesterol content is a key modulator of eukaryotic plasma membrane fluidity, with higher levels contributing to a less fluid and more rigid membrane. *T. brucei* bloodstream forms are auxotrophic for cholesterol, which is acquired from the mammalian host by receptor-mediated endocytosis (Smith and Bütikofer, 2010). Endocytic activity is not affected by *Tb*KIFC1 down-regulation (Vanwalleghem et al., 2015), and not surprisingly, neither the total cellular cholesterol content nor cholesterol/phospholipid ratio were affected by *Tb*KIFC1 depletion (Figure 5D). However, the cholesterol content of the plasma membrane of *TbKIFC1*^{RNAi} trypanosomes appeared to be higher than that of WT cells. For example, *TbKIFC1*^{RNAi} trypanosomes were more resistant to the toxic effect of the cholesterol-removing agent methyl-β-cyclodextrin (MBCD) (Figure 5E), which can increase membrane fluidity following even a modest reduction of cholesterol, as shown by FRAP experiments (Figure 5F).

The relative distribution of fluorescent cholesterol (Top Fluor) was employed to assess the levels of cholesterol co-localizing with trafficking compartments involved in vesicular routing to the cellular surface, between the nucleus-proximal Golgi and the kinetoplast-proximal flagellar pocket (Figure 6A). To measure cholesterol associated with the plasma membrane, we quantified the fluorescence of the membrane portion co-localizing with the mCherry-FAZ1 fusion protein (Figure 6A). This fluorescence was around 10% higher in *TbKIFC1*^{RNAi} cells than in WT cells, and this measurement was used as a control in all subsequent experiments. Quantitative analysis of cholesterol fluorescence in vesicular compartments revealed an altered distribution of cholesterol in *TbKIFC1*^{RNAi} cells relative to WT trypanosomes (Figure 6B). Cholesterol in *TbKIFC1*^{RNAi} cells appeared to be more prominently associated with the Golgi (around 20%–25% increase), using as Golgi markers the General Receptor for phosphoinositides 1-Associated Scaffold Protein (GRASP) and the coatomer β′ (β′ COP: see Figure S7 for β′ COP association with the Golgi). In contrast, it was less prominent (around 10% decrease) in the post-Golgi compartment involved in exocytosis (Rab11, Sec15 and Sec1 markers: Gabernet-Castello et al., 2011) (Figure 6). Thus, knockdown of *Tb*KIFC1 leads to cholesterol accumulation in both Golgi and plasma membrane (as measured here along the FAZ), together with reduction of cholesterol associated with exocytosis. These data suggest that *Tb*KIFC1 plays a role in the traffic of cholesterol-containing membranes within the parasite and that loss of *Tb*KIFC1 causes an increase in the cholesterol content of the Golgi and surface membranes. Since cholesterol is known to inhibit membrane fission and promote membrane fusion (Najafinobar et al., 2016; Yang et al., 2016), the accumulation of cholesterol in Golgi membranes of *TbKIFC1*^{RNAi} cells might account for the observed enlargement of Golgi cisternae in these cells (Figure 7A). Given the inhibition of fission in the secretory pathway, the TGN compartment increased in size, giving rise to unresolved flat cisternae and accumulation of clathrin-coated pits (Figure 7B). In the plasma membrane, the increase of cholesterol content is expected to reduce membrane fluidity, with major implications for growth in the mammalian host, but not *in vitro*.

DISCUSSION

The kinesin *Tb*KIFC1 is a surprising protein for many reasons. Originally linked with acidocalcisome traffic (Dutoya et al., 2001), it was later shown to play a key role in human innate immunity to *T. brucei* because of its function in the trafficking of the host-derived trypanolytic factor APOL1 within the parasite (Pays et al., 2014; Vanhamme et al., 2003; Vanhollebeke et al., 2008; Vanwalleghem et al., 2015). These functions fit with the widespread distribution of *Tb*KIFC1 throughout the cell, along with some concentration in the posterior region associated with vesicle traffic (Figure S2). Here we report another, unexpected role for *Tb*KIFC1: it is essential for parasite evasion of the mammalian adaptive immune response. Specifically, we propose that *Tb*KIFC1-mediated intracellular traffic is required to maintain appropriate levels of cholesterol in the surface membrane and a corresponding level of membrane fluidity that allows for a rapid clearance of VSG-antibody complexes from this surface. The VSG surface coat of African trypanosomes operates close to its molecular crowding threshold, yet the lateral mobility and mobile fraction of VSG in this membrane are very high (Hartel et al., 2016). Both these parameters depend on the composition and physical properties of the

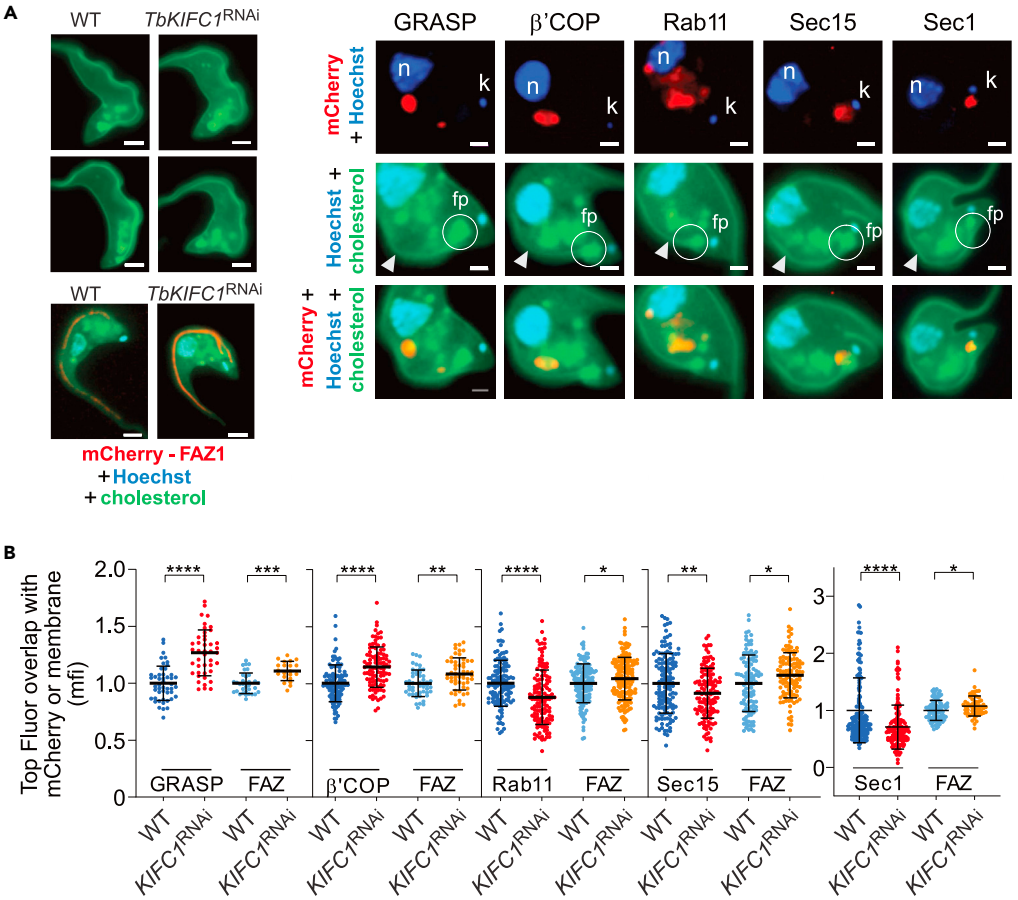

Figure 6. Role of TbKIFC1 in Cholesterol Trafficking to the Cell Surface

(A) Left panel: global fluorescence of WT and *TbKIFC1*^{RNAi} parasites after incubation for 60 min in Top Fluor Cholesterol, and relative co-localization of the flagellum-associated Top Fluor fluorescence with mCherry-tagged FAZ (scale bar = 2 μm). Right panel: intracellular localization in WT trypanosomes of Top Fluor cholesterol and different markers of intracellular traffic to the plasma membrane, tagged with mCherry (GRASP and β′COP for the Golgi, Rab11 for recycling endosomes and exocyst, Sec15 and Sec1 for the exocyst). The arrows designate the flagellum-associated Top Fluor labeling, apparently co-localizing with the FAZ (scale bar = 1 μm; n, nucleus and k, kinetoplast, both stained in blue with Hoechst; fp, flagellar pocket).

(B) Relative levels of cholesterol mean fluorescence intensity (mfi) after 60 min Top Fluor cholesterol uptake without prior cholesterol starvation, measured as either co-localizing with the FAZ as marker of the cell surface or co-localizing with fluorescence of mCherry conjugated with different intracellular markers (Golgi GRASP and β′COP, recycling endosomes/exocyst Rab11 or exocyst Sec15 and Sec1). Top Fluor fluorescence was measured within the exact surface of mCherry fluorescence. As internal reference for each trypanosome preparation, Top Fluor measurement in the FAZ region (similar surface in the different cells) was performed together with each of the mCherry measurements. Data are represented as mean ± SD; n = 3. Mann-Whitney test *p < 0.05; **p < 0.01; ***p < 0.001; ****p < 0.0001.

surface membrane (Hartel et al., 2016), and changes in the cholesterol content of this membrane could dramatically affect the mobility of VSG-antibody complexes. A stiffer, less fluid surface membrane in *Tb*KIFC1 knockdown parasites results in a slower clearance of these complexes from the trypanosome surface and consequently they cannot infect the mammalian host unless antibody synthesis is compromised. Our data demonstrate that clearance of surface-bound antibodies by trypanosomes is physiologically relevant, being required for mammalian infectivity, and that high VSG mobility in the surface membrane is critical for rapid clearance. Evidence suggests that trypanosome motility may drive directional movement of VSG-antibody complexes on the surface (Cheung et al., 2016; Engstler et al., 2007; O'Beirne et al., 1998), so the motility defect present in *TbKIFC1*^{RNAi} cells may contribute to slower clearance of VSG-antibody complexes. The idea of hydrodynamic flow-mediated sorting of antibody-VSG complexes (Engstler et al., 2007) is attractive, but an essentially immotile trypanosome, the dynein LC1-double knock-in (DKI) mutant, can

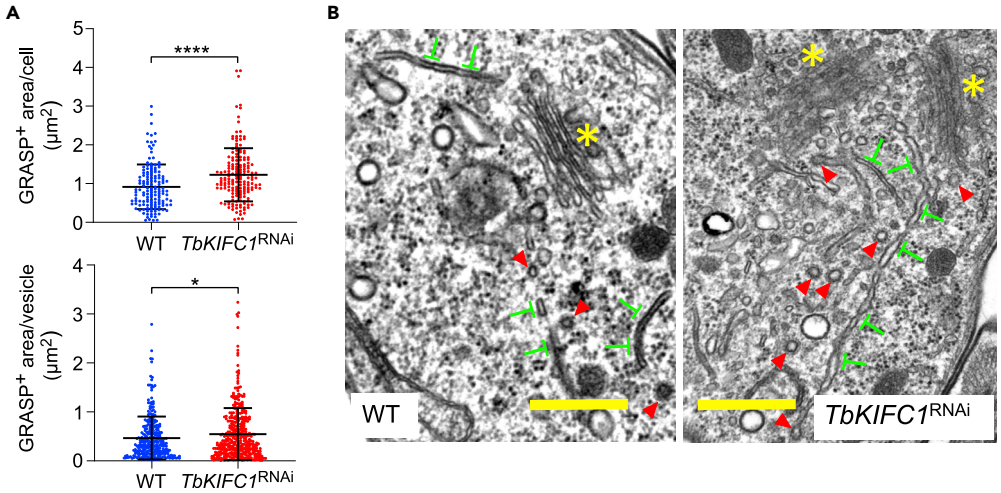

Figure 7. Cholesterol Traffic and Golgi Structure in *TbKIFC1*^{RNAi} Trypanosomes

(A) Size of GRASP^{+} compartments (by vesicle or by cell) in WT and *TbKIFC1*^{RNAi} trypanosomes. Data are represented as mean ± SD; n = 3. Mann-Whitney test *p < 0.05; ****p < 0.0001.

(B) Transmission electron microscopy analysis of WT and *TbKIFC1*^{RNAi} trypanosomes. Yellow asterisks and red arrows, respectively, label the *cis*-Golgi and clathrin-coated vesicles, and inverted green "T"s designate TGN-issued secretory vesicles that appear unprocessed in *TbKIFC1*^{RNAi} trypanosomes, therefore accumulating and increasing in size in these cells (scale bar = 500 nm).

clear VSG-IgG complexes from the surface at the same rate as WT parasites (Shimogawa et al., 2018). In the case of *TbKIFC1*^{RNAi} cells the motility effect appears very minor, so the slower rate of clearance of VSG-antibody complexes is probably due mainly to the decreased VSG mobility in a surface membrane with a higher cholesterol content. Interestingly, as observed for *TbKIFC1*^{RNAi} cells, the immotile mutants of Shimogawa et al. (2018) could not infect mice unless antibody synthesis was compromised. Therefore, *TbKIFC1*^{RNAi} cells are trypanosomes with essentially normal motility but impaired clearance of VSG-antibody complexes, whereas LC1-DKI cells are the reverse, immotile trypanosomes that clear surface-bound antibodies normally. It seems that clearance of surface-bound antibodies and motility are separate virulence factors in trypanosomes and both are required to overcome the host adaptive immune response.

The first responder here is IgM, and clearance of this immunoglobulin from the surface seems particularly important for trypanosomes. Anti-VSG IgM antibodies are detectable, albeit at low levels, as early as 3 days after infection (O'Beirne et al., 1998). Therefore, removal of VSG-IgM complexes must be important early in the infection. This may explain why no parasites were detected in *TbKIFC1*^{RNAi} infections of WT mice at day 3. Moreover, it is striking that IgMs are cleared from the surface of trypanosomes far faster than IgGs (Engstler et al., 2007) and the deleterious effect of *Tb*KIFC1 knockdown on clearance of antibodies appears more pronounced for IgMs than IgGs. It is tempting to speculate that clearance of immunoglobulins from the surface of trypanosomes is primarily designed to ensure that IgMs spend as little time on the surface as possible. One reason might be that IgMs are more efficient than IgGs at activating the complement system and failure to clear IgMs efficiently renders the trypanosome vulnerable to complement attack. There is indirect evidence to support this view, as the virulence defect in *TbKIFC1*^{RNAi} cells was not rescued in mice treated with clodronate liposomes to deplete mononuclear phagocytes. Interestingly too, non-dividing stumpy bloodstream forms, which clear VSG-antibody complexes even faster than slender forms because of their intrinsically higher rate of endocytosis (Engstler et al., 2007), are much less sensitive to complement-mediated lysis than slender forms (McLintock et al., 1993). So, rapid clearance of surface antibodies may have evolved to protect the trypanosome from IgM-mediated complement lysis.

Why does VSG switching not obviate the need for clearance of surface-bound antibodies in order to infect a mammalian host? The most likely reason is that VSG is an extremely abundant and stable protein, 10^7 copies per cell with a half-life of over 200 h (Engstler et al., 2004; Seyfang et al., 1990). Thus, previously expressed VSG could persist for some time on the surface of trypanosomes that have switched VSG. This issue was investigated by Pinger et al. (2018), using trypanosome clones expressing two VSGs at varied ratios,

representing parasites at multiple stages of VSG coat replacement. These parasites were used for *in vivo* infection assays in mice previously immunized against the titrating VSG. This study indicated that the previously expressed VSG could persist for some time on the surface of trypanosomes after a switch, but that there was only a narrow time period post switch when the switchers remained vulnerable to IgMs. This period was estimated to be up to 29 h after the switch event, when the level of the previously expressed VSG remained above somewhere between 1.3% and 7.6% of the total surface VSG. They proposed that below this antigen density the efficacy of IgM binding is reduced below a threshold level. Interestingly, the experiments of Pinger et al. (2018) were performed in mice immunized against the titrating VSG and so, the assay examined the effect of a high titer of IgM antibody as VSG antigen density decreased. A more natural situation would be increasing antibody levels as the level of the previously expressed VSG in the switcher decreases, and it is here that clearance of surface-bound IgM is likely to have a key role. Clearance assays show that, as antibody titers rise, clearance of surface-bound antibody gets progressively slower until eventually the system is overwhelmed because of the amount of IgM bound to VSG, which is what happens with the non-switchers. However, in a natural infection, as the level of IgMs increases over time the level of the previously expressed VSG in switchers is decreasing, so IgM-VSG complexes can still be efficiently cleared from these trypanosomes. Therefore, antibody clearance, and specifically clearance of surface-bound IgMs, protects trypanosomes at low antibody levels and high surface antigen density, e.g., early in the infection or shortly after a VSG switch, and also as the antibody levels increase and antigen density decreases as switchers divide, e.g., during the period from about 29 h after the switch until complete replacement of the VSG coat at 5–6 days. We propose that, when clearance of antibody-VSG complexes is compromised, as occurs in *TbKIFC1*^{RNAi} cells, both these groups become vulnerable to immune attack and therefore infection cannot develop.

It is important to note that the movement of VSG-antibody complexes is slower in *TbKIFC1*^{RNAi} cells because, as shown by photobleaching experiments, the lateral mobility of all VSGs is lower in these cells. Unlike non-bound VSG, VSG-antibody complexes are selectively sorted and concentrated toward the flagellar pocket/posterior end of the cells, in a process that is slowed down in *TbKIFC1*^{RNAi} cells because the membrane is less fluid. Internalization of VSG is not dependent on the mobility of an individual VSG but rather depends on the rate of membrane uptake from the surface through the flagellar pocket. As the VSG density appears to be unchanged in *TbKIFC1*^{RNAi} cells, the bulk VSG uptake is not expected to be affected in these cells, as indeed observed.

Although the known role of *Tb*KIFC1 was limited to the transport of acidocalcisomes and APOL1 (Dutoya et al., 2001; Pays et al., 2014; Vanwalleghem et al., 2015), the widespread intracellular distribution of this kinesin (Dutoya et al., 2001; Figure S2) suggested an important function in intracellular traffic. So how might this intracellular activity of *Tb*KIFC1 affect surface membrane fluidity/rigidity? Our data indicated that knockdown of *Tb*KIFC1 leads to higher cholesterol levels in both Golgi and plasma membrane, with a concomitant reduction in cholesterol levels in membranes associated with exocyst components such as Sec15 and Sec1. Therefore, we suggest that *Tb*KIFC1 is involved in the homeostasis of membrane cholesterol content and that the absence of this kinesin alters the balance of cholesterol flow between the intracellular and surface membranes.

Several observations are consistent with a role for *Tb*KIFC1 in intracellular cholesterol traffic. First, the *Tb*KIFC1 VHS domain interacted much better with anionic membranes when cholesterol was present. In particular, helix 7 of the VHS, which appears to interact directly with membranes, contains a motif for cholesterol binding (CARC) (Fantini and Barrantes, 2013). This motif is known to exhibit high affinity for cholesterol when the latter is present in the outer leaflet of membrane bilayers (Di Scala et al., 2017), which corresponds to the topology of the VHS/membrane interface. Moreover, the essential tyrosine of this CARC motif belongs to the residues whose mutations in the VSH7 mutant resulted in the loss of *Tb*KIFC1 membrane-trafficking activity. Second, the VHS domain of *Tb*KIFC1 may influence endosome trafficking, as suggested by observations made on the VHS domain of the adaptor protein Target of Myb protein 1 (TOM1), whose structure was used here as template for the modeling of the *Tb*KIFC1 VHS given its similarity with this domain. Indeed, the TOM1 VHS, which binds to phosphoinositides like the *Tb*KIFC1 VHS, was reported to influence endosome trafficking (Boal et al., 2015). Third, *Tb*KIFC1 is clearly involved in the intracellular transport of APOL1 (Vanwalleghem et al., 2015), which is associated with cholesterol in the high-density lipoproteins (HDL3) particles taken up into the parasite by receptor-mediated endocytosis (Vanhollebeke et al., 2008). It is possible that this cholesterol remains associated with APOL1 in endosomal

membranes and is subsequently trafficked by *Tb*KIFC1 within the parasite. Finally, within the *Tb*KIFC1-proximal proteome we identified *Tb*VPS4 together with a katanin containing a VPS4 oligomerization domain, and VPS4 is known to be involved in endosomal cholesterol trafficking in both mammals and protozoa (Bishop and Woodman, 2000; Du et al., 2013; Yang et al., 2004). Therefore, we propose that *Tb*KIFC1 is involved in moving membranes rich in cholesterol, most likely from endosomal compartments to other intracellular membranes. Suppression of this traffic would cause an increased flow of cholesterol to the surface through other routes, such as the recycling pathway from the Golgi. This redistribution is expected to give rise to a less fluid, stiffer surface membrane, as we observed in *TbKIFC1*^{RNAi} cells.

It has long been recognized that preventing or disruption of antigenic variation represents an ideal way to prevent/treat trypanosomiasis as the parasites would then become vulnerable to the host immune response. Our data suggest that drugs designed to inhibit *Tb*KIFC1 activity and disrupt clearance of surface bound antibodies could be a simpler way to achieve the same goal.

Limitations of the Study

This work did not allow fully detailed description of the pathway of cholesterol trafficking in the trypanosome, as we only document that *Tb*KIFC1 knockdown alters the balance of cholesterol flow between the intracellular and surface membranes.

Resource Availability

Lead Contact

Further information and requests for resources and reagents should be directed to and will be fulfilled by the Lead Contact, Etienne Pays (epays@ulb.ac.be).

Materials Availability

All unique/stable reagents generated in this study are available from the Lead Contact with a completed Materials Transfer Agreement. However, we only have a very limited amount of anti-VSG IgMs.

Data and Code Availability

The published article includes all proteomic data generated or analyzed during this study.

METHODS

All methods can be found in the accompanying Transparent Methods supplemental file.

SUPPLEMENTAL INFORMATION

Supplemental Information can be found online at https://doi.org/10.1016/j.isci.2020.101476.

ACKNOWLEDGMENTS

We thank V. Flamant for the gift of μMT KO mice, S. Dean for the gift of pPOTv7 plasmid, A. Gauquier for help in the BL approach, and D. Monteyne for SEM analysis. This work was supported by the European Research Council (ERC 669007-APOLs), the "Action de Recherches Concertées" of the University of Brussels (ULB) (ARC ADV), and the Fonds de la Recherche Scientifique (F.R.S.-FNRS) (PDR T.0159.13 to D.P.-M and PDR T.1003.14 to L.Lins and M.Deleu). The Center for Microscopy and Molecular Imaging is supported by the European Regional Development Fund and Wallonia. C.Y.B. and Y.Y. are supported by the Atip-Avenir and Fondation FINOVI programs (CNRS-INSERM-Finovi Atip-Avenir Apicolipid projects), and the Laboratoire d'Excellence Parafrap, France (grant number ANR-11-LABX-0024). Computational resources have been provided by the Consortium des Equipements de Calcul Intensif (CECI), funded by the FNRS (Grant No. 2.5020.11). D.P.N. thanks the Wellcome Trust and Science Foundation Ireland (SFI) for financial support. M.D. and L.L. thank the FRS-FNRS for their positions as Senior Research Associates.

AUTHOR CONTRIBUTIONS

E.P., D.P.N. and L. Lecordier designed the research; L. Lecordier, S.U., G.V., M.Deleu, J.-M.C., P.B., B.M., A-C.D., Y.Y., M.Dieu, P.T., D.P.-M., and D.P.N. performed the research; B.V., L. Lins, C.Y.B., D.A., Y.D., D.P.-M., and D.P.N. supervised some aspects of the work; E.P. and D.P.N. wrote the paper.

DECLARATION OF INTERESTS

The authors declare that they have no competing financial interest.

Received: December 13, 2019
Revised: July 30, 2020
Accepted: August 17, 2020
Published: September 25, 2020

REFERENCES

Arnold, K., Bordoli, L., Kopp, J., and Schwede, T. (2006). The SWISS-MODEL Workspace: a web-based environment for protein structure homology modelling. Bioinformatics *22*, 195–201.

Barry, J.D. (1979). Capping of variable antigen on *Trypanosoma brucei*, and its immunological and biological significance. J. Cell Sci. *37*, 287–302.

Bishop, N., and Woodman, P. (2000). ATPase-defective mammalian VPS4 localizes to aberrant endosomes and impairs cholesterol trafficking. Mol. Biol. Cell *11*, 227–239.

Boal, F., Mansour, R., Gayral, M., Saland, E., Chicanne, G., Xuereb, J.M., Marcellin, M., Burlet-Schiltz, O., Sansonetti, P.J., Payrastre, B., et al. (2015). TOM1 is a PI5P effector involved in the regulation of endosomal maturation. J. Cell Sci. *128*, 815–827.

Cheung, J.L., Wand, N.V., Ooi, C.P., Ridewood, S., Wheeler, R.J., and Rudenko, G. (2016). Blocking synthesis of the Variant Surface Glycoprotein coat in *Trypanosoma brucei* leads to an increase in macrophage phagocytosis due to reduced clearance of surface coat antibodies. PLoS Pathog. *12*, e1006023.

Di Scala, C., Baier, C.J., Evans, L.S., Williamson, P.T.F., Fantini, J., and Barrantes, F.J. (2017). Relevance of CARC and CRAC cholesterol-recognition motifs in the nicotinic acetylcholine receptor and other membrane-bound receptors. Curr. Top. Membr. *80*, 3–23.

Du, X., Kazim, A.S., Dawes, I.W., Brown, A.J., and Yang, H. (2013). The AAA ATPase VPS4/SKD1 regulates endosomal cholesterol trafficking independently of ESCRT-III. Traffic *14*, 107–119.

Dutoya, S., Gibert, S., Lemercier, G., Santarelli, X., Baltz, D., Baltz, T., and Bakalara, N. (2001). A novel C-terminal kinesin is essential for maintaining functional acidocalcisomes in *Trypanosoma brucei*. J. Biol. Chem. *276*, 49117–49124.

Engstler, M., Pfohl, T., Herminghaus, S., Boshart, M., Wiegertjes, G., Heddergott, N., and Overath, P. (2007). Hydrodynamic flow-mediated protein sorting on the cell surface of trypanosomes. Cell *131*, 505–515.

Engstler, M., Thilo, L., Weise, F., Grünfelder, C.G., Schwarz, H., Boshart, M., and Overath, P. (2004). Kinetics of endocytosis and recycling of the GPI-anchored variant surface glycoprotein in *Trypanosoma brucei*. J. Cell Sci. *117*, 1105–1115.

Fantini, F., and Barrantes, F.J. (2013). How cholesterol interacts with membrane proteins: an exploration of cholesterol-binding sites including CRAC, CARC, and tilted domains. Front. Physiol. *4*, 31.

Gabernet-Castello, C., Dubois, K.N., Nimmo, C., and Field, M.C. (2011). Rab11 function in *Trypanosoma brucei*: identification of conserved and novel interaction partners. Eukaryot. Cell *10*, 1082–1094.

Harrington, J.M., Widener, J., Stephens, N., Johnson, T., Francia, M., Capewell, P., Macleod, A., and Hajduk, S.L. (2010). The plasma membrane of bloodstream-form African trypanosomes confers susceptibility and specificity to killing by hydrophobic peptides. J. Biol. Chem. *285*, 28659–28666.

Hartel, A.J., Glogger, M., Jones, N.G., Abuillan, W., Batram, C., Hermann, A., Fenz, S.F., Tanaka, M., and Engstler, M. (2016). N-glycosylation enables high lateral mobility of GPI-anchored proteins at a molecular crowding threshold. Nat. Commun. *7*, 12870.

Hu, C.A., Klopfer, E.I., and Ray, P.E. (2012). Human apolipoprotein L1 (ApoL1) in cancer and chronic kidney disease. FEBS Lett. *586*, 947–955.

Krieg, M., Fläschner, G., Alsteens, D., Gaub, B.M., Roos, W.H., Wuite, G.J.L., Gaub, H.E., Gerber, C., Dufrêne, Y.F., and Müller, D.J. (2019). Atomic force microscopy-based mechanobiology. Nat. Rev. Phys. *1*, 41–57.

MacGregor, P., Szöőr, B., Savill, N.J., and Matthews, K.R. (2012). Trypanosomal Immune evasion, chronicity and transmission: an elegant balancing act. Nat. Rev. Microbiol. *10*, 431–438.

McLintock, L.M., Turner, C.M., and Vickerman, K. (1993). Comparison of the effects of immune killing mechanisms on *Trypanosoma brucei* parasites of slender and stumpy morphology. Parasite Immunol. *15*, 475–480.

Najafinobar, N., Mellander, L.J., Kurczy, M.E., Dunevall, J., Angerer, T.B., Fletcher, J.S., and Cans, A.S. (2016). Cholesterol alters the dynamics of release in protein independent cell models for exocytosis. Sci. Rep. *6*, 33702.

Nasir, M.N.N., Lins, L., Crowet, J.M., Ongena, M., Dorey, S., Dhondt-Cordelier, S., Clément, C., Bouquillon, S., Haudrechy, A., Sarazin, C., et al. (2017). Differential interaction of synthetic glycolipids with biomimetic plasma membrane lipids correlates with the plant biological response. Langmuir *33*, 9979–9987.

O'Beirne, C., Lowry, C.M., and Voorheis, H.P. (1998). Both IgM and IgG anti-VSG antibodies initiate a cycle of aggregation-disaggregation of bloodstream forms of *Trypanosoma brucei* without damage to the parasite. Mol. Biochem. Parasitol. *91*, 165–193.

Pays, E., Vanhollebeke, B., Uzureau, P., Lecordier, L., and Pérez-Morga, D. (2014). The molecular arms race between African trypanosomes and humans. Nat. Rev. Microbiol. *12*, 575–584.

Pérez-Morga, D., Vanhollebeke, B., Paturiaux-Hanocq, F., Nolan, D.P., Lins, L., Homblé, F., Vanhamme, L., Tebabi, P., Pays, A., Poelvoorde, P., et al. (2005). Apolipoprotein L-I promotes trypanosome lysis by forming pores in lysosomal membranes. Science *309*, 469–472.

Pinger, J., Chowdhury, S., and Papavasiliou, F.N. (2018). Variant surface glycoprotein density defines an immune evasion threshold for African trypanosomes undergoing antigenic variation. Nat. Commun. *8*, 828.

Roux, K.J., Kim, D.I., Raida, M., and Burke, B. (2012). A promiscuous biotin ligase fusion protein identifies proximal and interacting proteins in mammalian cells. J. Biol. Chem. *196*, 801–810.

Seyfang, A., Mecke, D., and Duszenko, M. (1990). Degradation, recycling, and shedding of *Trypanosoma brucei* variant surface glycoprotein. J. Protozool. *37*, 546–552.

Sharma, A.I., Olson, C.L., Mamede, J.I., Gazos-Lopes, F., Epting, C.L., Almeida, I.C., and Engman, D.M. (2017). Sterol targeting drugs reveal life cycle stage-specific differences in trypanosome lipid rafts. Sci. Rep. *7*, 9105.

Shimogawa, M.M., Ray, S.S., Kisalu, N., Zhang, Y., Geng, Q., Ozcan, A., and Hill, K.L. (2018). Parasite motility is critical for virulence of African trypanosomes. Sci. Rep. *8*, 9122.

Smith, T.K., and Bütikofer, P. (2010). Lipid metabolism in *Trypanosoma brucei*. Mol. Biochem. Parasitol. *172*, 66–79.

Uzureau, S., Coquerelle, C., Uzureau, P., Vermeiren, C., Pilotte, L., Van Acker, A., Acolty, V., Vanhollebeke, B., Van den Eynde, B., Moser, M., et al. (2016). Apolipoproteins L control cell death triggered by TLR3/TRIF signaling in dendritic cells. Eur. J. Immunol. *46*, 1854–1866.

Vanhamme, L., Paturiaux-Hanocq, F., Poelvoorde, P., Nolan, D.P., Lins, L., Van den Abbeele, J., Pays, A., Tebabi, P., Xong, H.V., Jacquet, A., et al. (2003). Apolipoprotein L-I is the trypanosome lytic factor of human serum. Nature *422*, 83–87.

Vanhollebeke, B., and Pays, E. (2006). The function of apolipoproteins L. Cell. Mol. Life Sci. *63*, 1937–1944.

Vanhollebeke, B., Demuylder, G., Nielsen, M.J., Pays, A., Tebabi, P., Dieu, M., Raes, M., Moestrup, S.K., and Pays, E. (2008). A haptoglobin-hemoglobin receptor conveys innate immunity to *Trypanosoma brucei* in humans. Science *320*, 677–681.

Vanwalleghem, G., Fontaine, F., Lecordier, L., Tebabi, P., Klewe, K., Nolan, D.P., Yamaryo-Botté, Y., Botté, C., Kremer, A., Schumann Burkard, G., et al. (2015). Coupling of lysosomal and mitochondrial membrane permeabilization in trypanolysis by APOL1. Nat. Commun. *6*, 8078.

Wan, G., Zhaorigetu, S., Liu, Z., Kaini, R., Jiang, Z., and Hu, C.A. (2008). Apolipoprotein L1, a novel Bcl-2 homology domain 3-only lipid-binding protein, induces autophagic cell death. J. Biol. Chem. *283*, 21540–21549.

Yang, M., Coppens, I., Wormsley, S., Baevova, P., Hoppe, H.C., and Joiner, K.A. (2004). The *Plasmodium falciparum* Vps4 homolog mediates multivesicular body formation. J. Cell Sci. *117*, 3831–3838.

Yang, S.T., Kreutzberger, A.J.B., Lee, J., Kiessling, V., and Tamm, L.K. (2016). The role of cholesterol in membrane fusion. Chem. Phys. Lipids *199*, 136–143.

iScience, Volume *23*

Supplemental Information

The *Trypanosoma Brucei* KIFC1 Kinesin Ensures the Fast Antibody Clearance Required for Parasite Infectivity

Laurence Lecordier, Sophie Uzureau, Gilles Vanwalleghem, Magali Deleu, Jean-Marc Crowet, Paul Barry, Barry Moran, Paul Voorheis, Andra-Cristina Dumitru, Yoshiki Yamaryo-Botté, Marc Dieu, Patricia Tebabi, Benoit Vanhollebeke, Laurence Lins, Cyrille Y. Botté, David Alsteens, Yves Dufrêne, David Pérez-Morga, Derek P. Nolan, and Etienne Pays

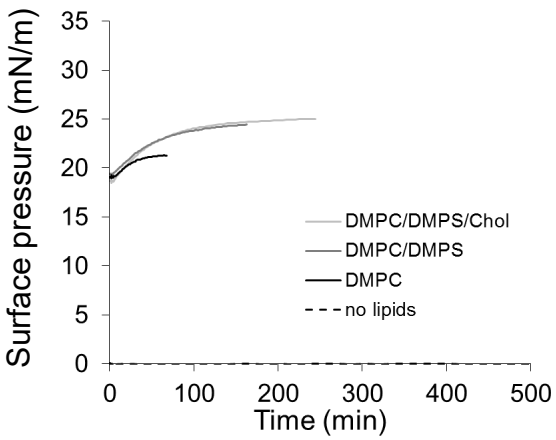

Figure S1*. Tb*KIFC1 interaction with synthetic membranes (related to Fig. 1)

Adsorption kinetics of the mutant VHS7 domain into an air-water interface (without lipids) or into a lipid monolayer composed by DMPC or DMPC-DMPS (1:1) or DMPC-DMPS-Cholesterol (1:1:2).

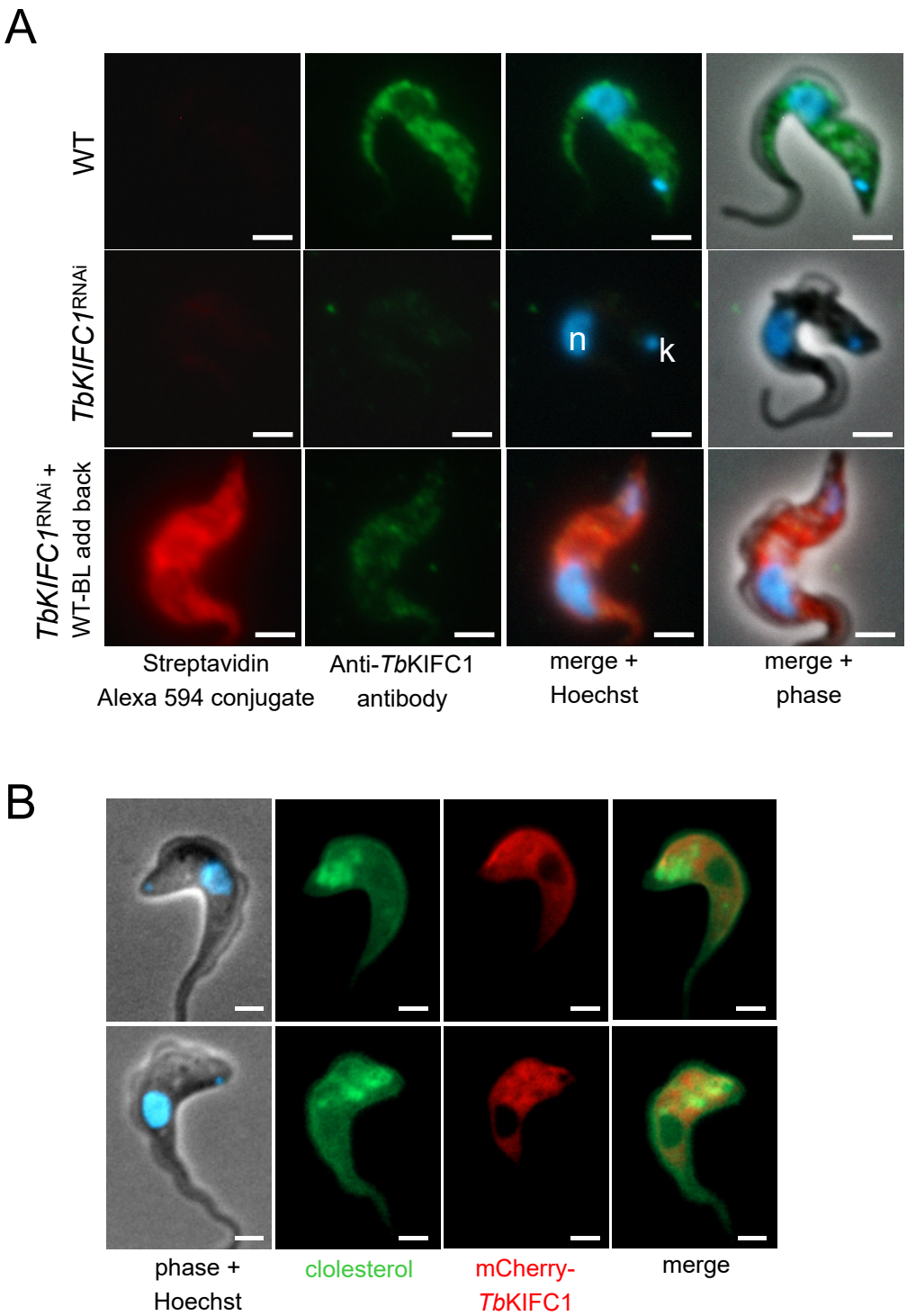

Figure S2. *Tb*KIFC1 expression (related to Fig. 1)

(A) Immunofluorescence analysis of *Tb*KIFC1 expression in WT and *TbKIFC1*^{RNAi} parasites, with or without addback expression of BL-WT *Tb*KIFC1. (n = nucleus; k = kinetoplast; bar = 2 μm)

(B) Localization of endogenously tagged mCherry-*Tb*KIFC1 in WT parasites labelled with Top Fluor cholesterol and Hoechst (bar = 2μm).

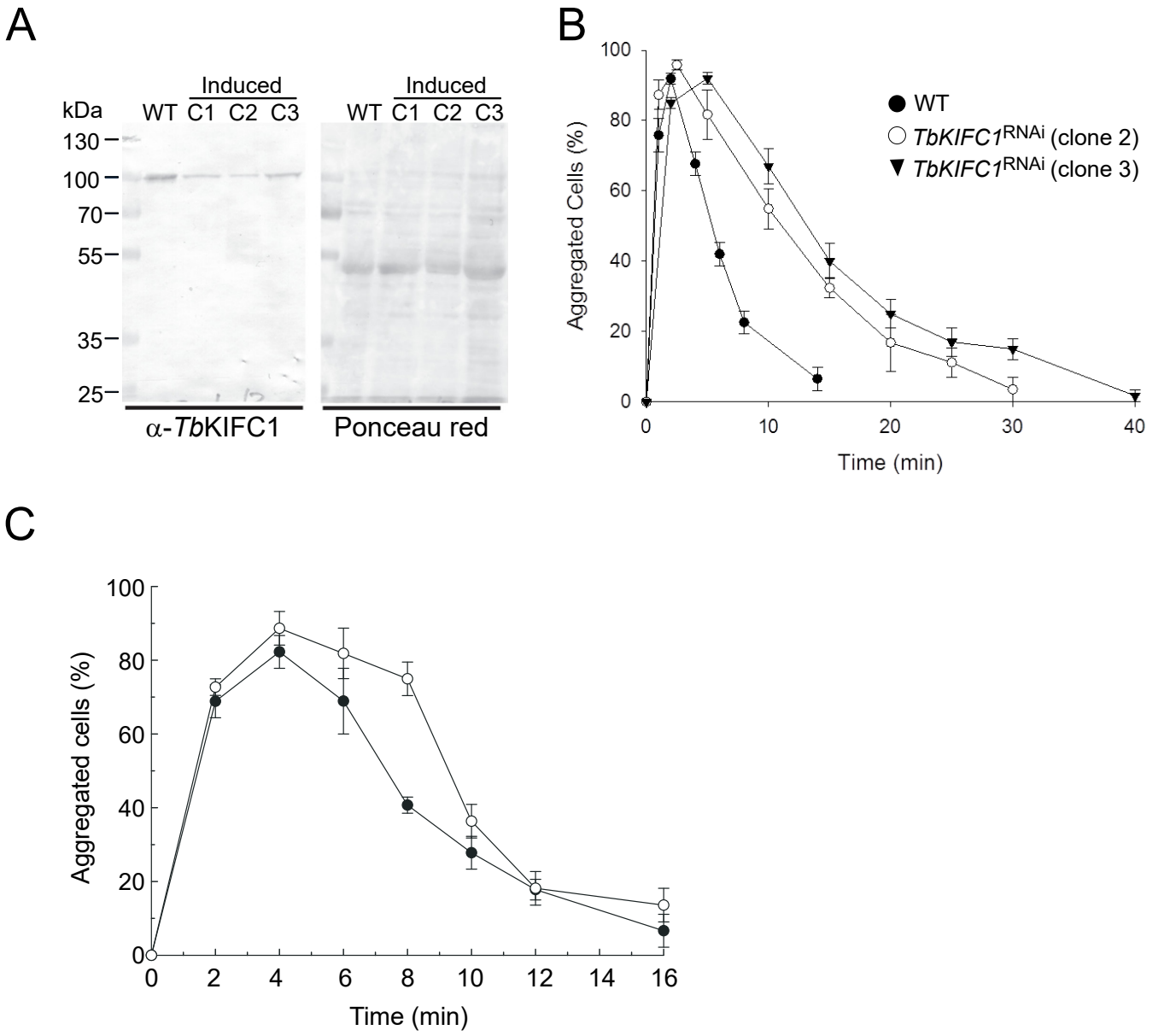

Figure S3. *Tb*KIFC1 levels in different cloned *TbKIFC1*^{RNAi} cell lines and kinetics of WT or *TbKIFC1*^{RNAi} parasite disaggregation following addition of anti-VSG IgGs or IgMs (related to Fig. 4)

(A) Western blot analysis of *Tb*KIFC1 levels (~ 100 kDa band) in WT and three different cloned *TbKIFC1*^{RNAi} cell lines (clones 1-3: C1, C2, C3) following 48 h of RNAi induction by doxycyclin.

(B) WT and two different *TbKIFC1*^{RNAi} cell lines (Clones 2 and 3 both 48 h induction by doxycyclin) were incubated with purified anti-VSG IgGs (1 µg/ml) and the clearance of surface-bound antibodies was monitored by a cell aggregation assay (error bars: S.D.; n=3).

(C) Kinetics of *TbKIFC1*^{RNAi} parasite disaggregation following addition of anti-VSG IgM. Two different *TbKIFC1*^{RNAi} cell lines, clones 2 (●) and 3 (○), both 48 h induction by doxycycline, were incubated with purified anti-VSG IgMs (4 µg/ml) and the clearance of surface-bound antibodies was monitored by a cell aggregation assay (error bars: S.D.; n=3).

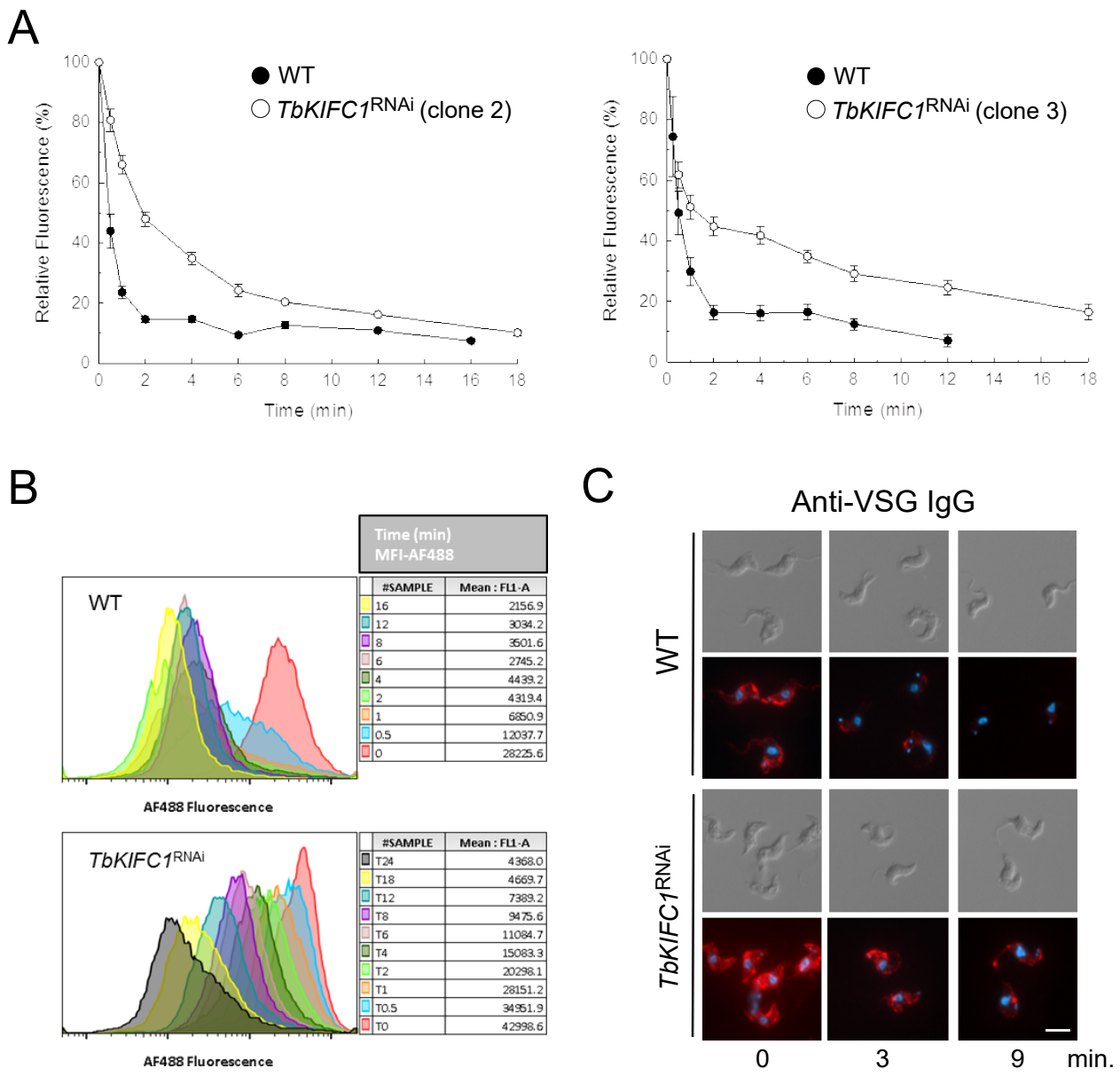

Figure S4. Clearance of VSG-IgG complexes from the surface of WT and *TbKIFC1*^{RNAi} cells (related to Fig. 4)

(A) Clearance of surface-bound antibodies (anti-VSG IgG) was determined by flow cytometry of WT and *TbKIFC1*^{RNAi} cells (clones 2 and 3 from Fig. S3, 48 h of RNAi induction by doxycyclin) incubated with anti-VSG immune serum. The data are expressed as % median fluorescence intensity detected relative to time zero (error bars: S.D.; n=3).

(B) WT and *TbKIFC1*^{RNAi} cells (clone 1, 48 h of RNAi induction by doxycyclin) were incubated with anti-VSG immune serum and the clearance of surface-bound antibodies was determined by flow cytometry. The panels show representative samples (data fromFig.3D) of individual fluorescence intensity distributions of surface Alex488 fluorescence *versus* cell count (total 10,000) at each time point.

(C) Fluorescence microscopy representative kinetics of clearance of anti MiTat 1.1 VSG IgGs from the surface of WT and *TbKIFC1*^{RNAi} (48 h induction) parasites. Cells were incubated for 30 min at 4°C with anti-VSG antibodies (IgG) and then incubated at 37°C for 0, 3 and 9 min. Surface-bound antibodies are revealed by immunofluorescence with Alexa 594 anti-rabbit secondary antibodies. bar = 5µm.

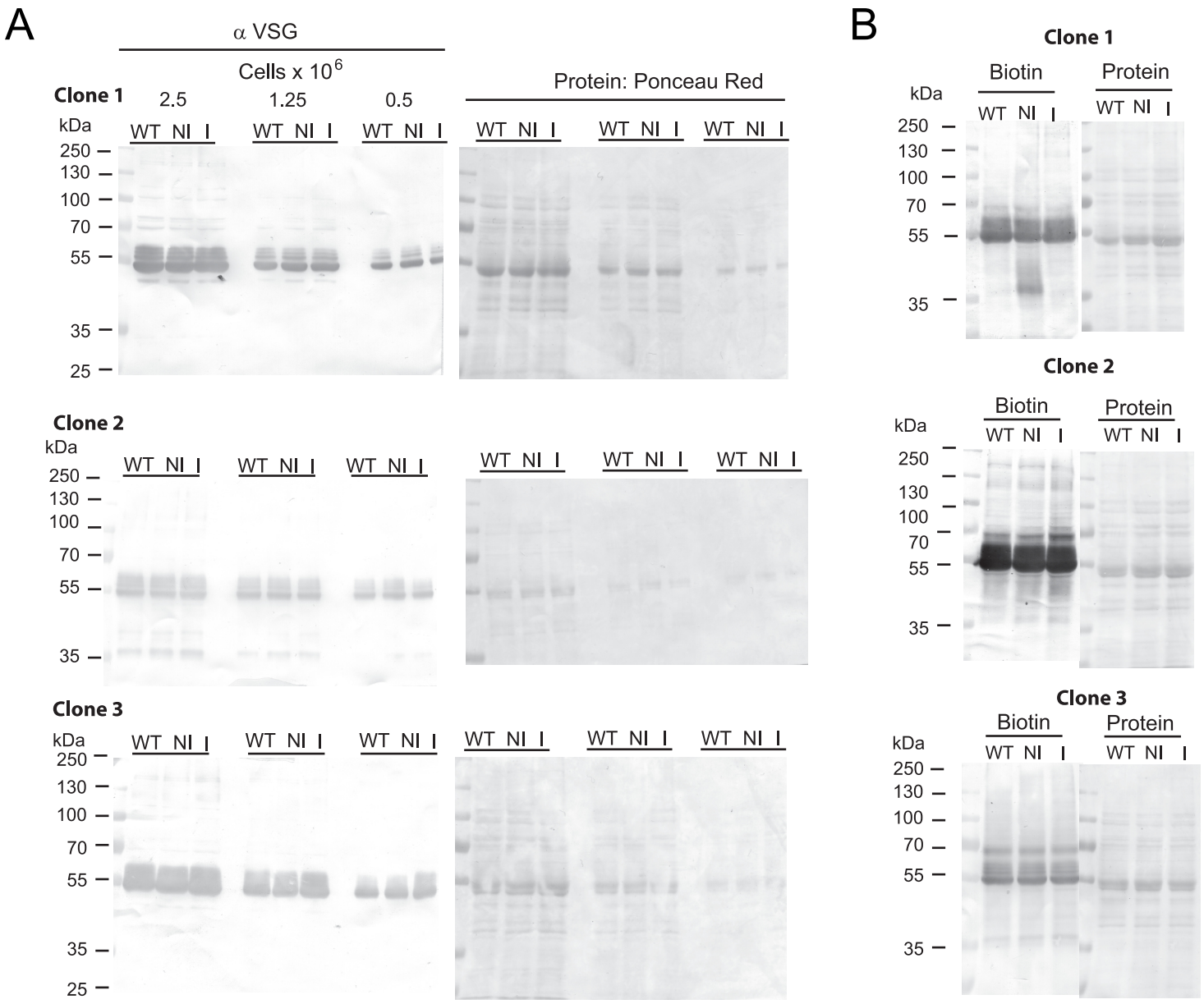

Figure S5. VSG titration and surface biotinylation in WT and *TbKIFC1*^{RNAi} cell lines (related to Fig. 4)

(A) Level of VSG expression, as determined by Western blotting using anti-MiTat 1.1VSG antibodies. Protein loading was assessed by Ponceau Red staining prior to blotting. Titrations were performed by loading various cell equivalents of WT, non-induced (NI) and induced (I) cells (48 h of RNAi induction by doxycyclin).

(B) Protein exposure on the parasite surface, as determined by surface biotinylation using non-cleavable EZ-link Sulfo-NHS-biotin. Biotinylated proteins were detected in samples (2.5 x 10^6 cells) of WT, non-induced (NI) and induced (I) *TbKIFC1*^{RNAi} cells (48 h of RNAi induction by doxycyclin) by streptavidin-AP blotting (left lanes in each panel). Protein loading was assessed by Ponceau Red staining prior to blotting (right lanes in each panel).

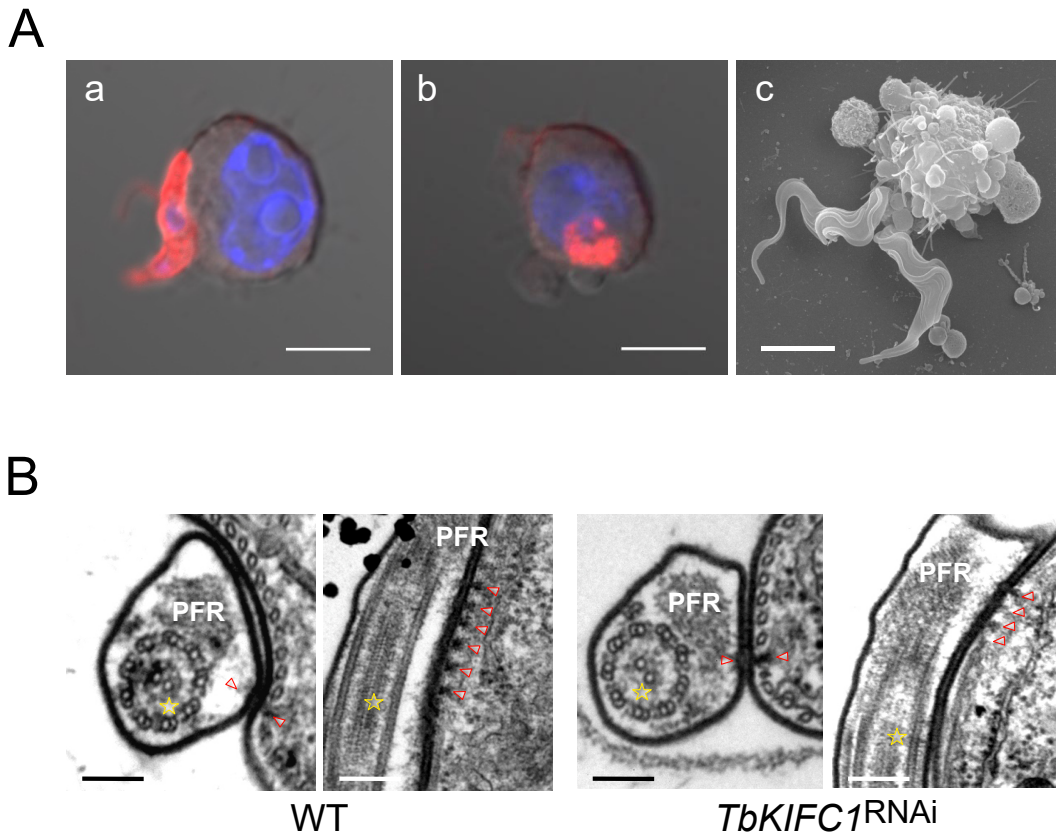

Figure S6. Phenotypic characteristics of *TbKIFC1*^{RNAi} parasites (related to Fig. 4)

(A) Uptake by macrophages. Representative IF and SEM images of macrophage-bound (a,c) or macrophage–phagocytosed (b) trypanosomes, after incubation for 30 min with anti-MiTat 1.1 VSG antibodies (red: anti-VSG antibodies; blue: nuclear DAPI staining; bar = 5µm).

(B) No alteration of the flagellum. TEM images of cross and longitudinal sections of the flagellum in WT and *TbKIFC1*^{RNAi} trypanosomes (star = axoneme; arrow point = FAZ filament; bar = 200 nm).

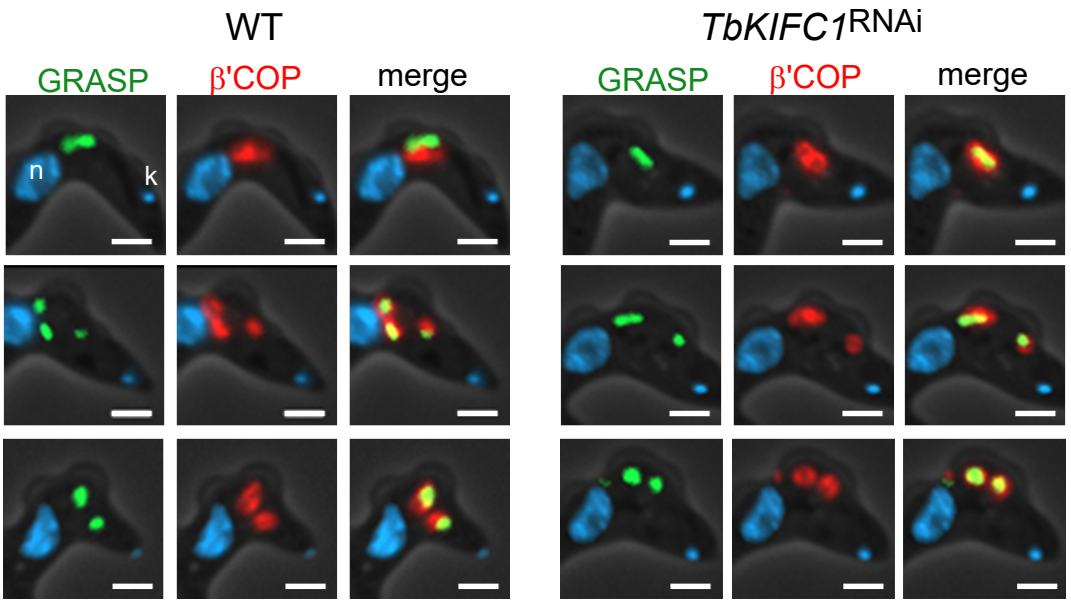

Figure S7. Association of β' COP with the Golgi (related to Fig. 6)

Fluorescence analysis of red mCherry-β'COP and green YFP-GRASP conjugates in WT and *TbKIFC1*^{RNAi} parasites (blue = Hoechst staining of DNA in nucleus (n) and kinetoplast (k)). (Bar = 2 μm)

Transparent Methods

Ethics statement. This research was approved by the ethics committee of the Institute for Molecular Biology and Medicine (IBMM). All mice were housed in our specified pathogen-free facility and the experiments were performed in compliance with the relevant laws and institutional guidelines (license LA1500474).

Parasites. *Trypanosoma brucei brucei* parasites were grown in HMI9 supplemented with 10% foetal bovine serum, 10% Serum Plus at 37°C in 5% CO_2. The 328-114 *TbKIFC1*^{RNAi} cell line and add backs were described previously (Vanwalleghem et al., 2015). A new *TbKIFC1*^{RNAi} cell line was generated using the SmOx plasmid (Poon et al., 2012), with the p2T7-177 vector and a MITat 1.1 *T. brucei* clone as the parental line. This MITat1.1 cell line was used in experiments with anti-VSG antibodies; clone 1 was used in most experiments, and two additional clones were used in experiments shown in supplemental figures. RNAi was induced by incubation with 1 µg/ml doxycycline for 48 h prior to experiments.

Production of recombinant WT and mutant VHS domain. The sequence encoding the VHS domain of *Tb*KIFC1 (amino acids 1 to 156) was amplified by PCR from recoded WT or VHS7 mutant *TbKIFC1* and inserted in the pStaby1.2 vector (Delphi Genetics) in fusion with the Histidine tag. Expression was induced overnight at 30°C with 1 mM isopropyl β-D-thiogalactoside. Recombinant proteins were purified from inclusion bodies (Vanhamme et al., 2003).

Binding of recombinant VHS to lipid strips. Lipid binding assays were performed on lipid-coated strips (Wan et al., 2008).

Molecular modelling of *Tb*KIFC1. The *Tb*KIFC1 sequence was aligned with that of the VHS domains of TOM1 (PDB code: 1ELK) and of the human signal transducing adaptor molecule 2 (1X5B). The *Tb*KIFC1 model was build using the SWISS model (Arnold et al., 2006).

Interaction of *Tb*KIFC1 helices H7H8 with POPS or POPC. Interaction of H7H8 with POPS/POPC was first simulated by a docking method as previously described (Deleu et al., 2014; Lins et al., 1999). Briefly, the position of the peptide stays still while the lipid molecule moves along and around it (more than 10^6 rotations and translations). For each position, the energy of interaction between the two molecules is calculated as the sum of Van der Waals, electrostatic and hydrophobic terms. The energy values together with the coordinates of all assemblies are stored in a matrix and classified according to decreasing values. The most stable matching is used to decide of the position of the first lipid. The position of the second lipid is then defined as the next most energetically favourable orientation stored in the hypermatrix taking steric and energetic constraints due to the presence of the first lipid molecule into account. For the next lipid molecule, the same process is repeated but the positions of all surrounding molecules are modified alternatively in order to find the lowest energy state. Five molecules of lipids (POPS or POPC) were docked around the peptide and the average interaction energy was calculated. To have a more realistic model, the interaction of *Tb*KIFC1 H7H8 with a POPC/POPS membrane was simulated by molecular dynamics. The peptide was first modeled in an atomistic representation. The martinize script (De Jong et al., 2013) was used to convert the structure to a coarse grained (CG) representation and to generate the topology for the MARTINI force field (Marrink et al., 2007; Monticelli et al., 2008). The CG peptide is placed in a simulation box with a POPC/POPS membrane (9:1

molar ratio) with the insane script (Ingolfsson et al., 2014). A 5000 steps steepest-descent energy minimization is performed to remove any steric clashes and a 1 μs production simulation is run. Temperature and pressure are coupled at 300 K and 1 bar using the weak coupling Berendsen algorithm (Berendsen et al., 1984) with $\tau T = 1$ ps and $\tau P = 1$ ps. Pressure is coupled semi-isotropically. Non bonded interactions are computed up to 1.2 nm with the shift method. Electrostatics are treated with $\varepsilon = 15$ and compressibility is 10^5 (1/bar). CG simulations have been carried out by using Gromacs 4.5.4 (Hess et al., 2008). At the end of simulation, the system is transformed to an atomistic resolution with the reverse script (Wassenaar et al., 2014) and all atom MD is further performed with Gromos G54a7 force field (Schmid et al., 2011). All the systems studied are first minimized by steepest descent for 5000 steps. A 100 ps simulation is run with the peptide under position restraints and NVT conditions, followed by a 1 ns simulation with the peptide under position restraints and NPT conditions. Production simulations of 250 ns are performed. Periodic boundary conditions (PBC) are used with a 2 fs time step. All the systems are solvated with SPC water (Hermans et al., 1984) and MD runs are carried out in NPT conditions (298 K and 1 bar). Temperature is maintained by using the v-rescale method (Bussi et al., 2007) with $\tau T = 0.2$ ps and isotropic pressure by using Berendsen barostat (Berendsen et al., 1984), with a compressibility of 10^5 (1/bar) and $\tau P = 1$ ps. Electrostatic interactions are treated by using the particle mesh Ewald (PME) method (Essmann et al., 1995) van der Waals and electrostatics are treated with a 1.0 nm cut-off. Bond lengths are maintained with the LINCS algorithm (Hess et al., 1997). Trajectories were analyzed with GROMACS 4.5.4 tools as well as with homemade scripts and softwares. 3D structures were analyzed with PyMOL (Schrödinger, 2010) and VMD (Humphrey et al., 1996) softwares.

***Tb*KIFC1 VHS, VHS7 and H7H8 adsorption on lipid monolayers.** Adsorption experiments of either recombinant *Tb*KIFC1 VHS and VHS7 domain or synthetic H7H8 peptide to air-aqueous medium interface in the absence or presence of DMPC, DMPC-DMPS (1:1) or DMPC-DMPS-cholesterol (1:1:2) membranes were performed in a KSV Minitrough (9.5 cm x 21 cm) equipped with a Wilhelmy plate. The sub-phase was 10 mM Tris-HCl (pH 7.4) and temperature was maintained at 22 ± 1°C during all experiments. The sub-phase was continuously stirred. Lipids were spread at the air-water interface to reach the desired initial surface pressure (Π_i ~18.5 mN/m). 30 min-waiting was required for solvent evaporation and film stabilization. *Tb*KIFC1 VHS or H7H8, dissolved in DMSO at $12.4.10^{-5}$ M, was then injected (20 µL) underneath the pre-formed lipid monolayer (final concentration in sub-phase: $3.09.10^{-8}$ mol/L and 0.59×10^{-6} mol/L for VHS and H7H8 respectively) and its adsorption was followed by tensiometry as an increase of surface pressure (Nasir et al., 2017). No change of the surface pressure was observed after injection of DMSO. The attractiveness factor is defined as $(\Delta\Pi_0 - \Delta\Pi_x)/\Delta\Pi_x$ with $\Delta\Pi_0$ corresponding to the y-intercept of the linear regression of $\Delta\Pi_{eq}$ vs Π_i, and $\Delta\Pi_x$, which is the equilibrium surface pressure increase without lipid monolayer. The uncertainties of the maximal insertion pressures (MIP) and of the attractiveness factor were calculated using IgoPro Software.

Construction of Biotin Ligase (BL)-conjugated *Tb*KIFC1. The Biotin Ligase (BL) gene (BirA*) gene was inserted by recombination in the recoded addback versions of WT and VHS7 *TbKIFC1* genes in order to fuse the BL domain between amino acids 379 and 380 of *Tb*KIFC1, within a poly-proline stretch. The two constructs were transfected in *TbKIFC1*^{RNAi} trypanosomes that were selected for hygromycin resistance. Resistant parasites were analysed for expression and functionality of the *Tb*KIFC1-BL fusion protein by *TbKIFC1* qRT-PCR and lysis test with APOL1. Biotinylation activity of the fusion protein was verified after 24h

incubation with 1 µg/ml doxycycline and 50 µM Biotin, by Western blot revealed with Streptavidin-peroxydase and chemioluminescence, and by immunofluorescence with streptavidin-Alexa-594.

Mass spectrometry analysis of *Tb*KIFC1-BL proteins bound to streptavidin. WT parasites, WT and VHS7 *Tb*KIFC1-BL addback cells were incubated for 24 h with 1 µg/ml doxycycline before addition of 50 µM biotin for further 24 h. Parasites were lysed in phosphate-buffered saline (PBS) containing 1% NP40, 0.25% Na-deoxycholate and 0.2% SDS for 1 h on ice, and the lysates were cleared by centrifugation at 21,000 g. The supernatants were incubated for 2 h at 4°C with streptavidin agarose beads (Pierce). The beads were washed three times with lysis buffer and twice with PBS buffer. Proteins were eluted from beads by boiling for 5 min in Laemmli sample buffer containing 1 mM biotin, and separated by SDS PAGE. Each lane was analysed by mass spectrometry after tryptic digestion. The peptides were analyzed using nano-LC-ESI-MS/MS maXis Impact UHR-TOF (Bruker, Bremen, Germany) coupled with a UPLC Dionex UltiMate 3000 (Thermo). The lanes were excised from SDS PAGE gels, and the proteins were digested with trypsin by in-gel digestion. The gel pieces were washed twice with distilled water and then shrunk with 100 % acetonitrile. Proteolytic digestion was performed by the addition of 6 µl of modified trypsin (Promega) suspended in 50 mM NH_4HCO_3 cold buffer. Proteolysis was performed overnight at 37°C. The supernatants were collected and the eluates were kept at – 20°C prior to analysis. The digests were separated by reverse-phase liquid chromatography using a 75 µm X 250 mm reverse phase Thermo column (Acclaim PepMap 100 C18) in an Ultimate 3000 liquid chromatography system. Mobile phase A was 95 % of 0.1 % formic acid in water and 5 % acetonitrile. Mobile phase B was 0.1 % formic acid in acetonitrile. The digests (15 µl) were injected, and the organic content of the mobile phase was increased linearly from 4 % B to 35

% in 35 min and from 35 % B to 90 % B in 5min. The column effluent was connected to a Captive Spray (Bruker). In survey scan, MS spectra were acquired for 0.5 s in the m/z range between 50 and 2200. The 10 most intense peptides ions 2^+ or 3^+ were sequenced. The collision-induced dissociation (CID) energy was automatically set according to mass to charge (m/z) ratio and charge state of the precursor ion. MaXis and Thermo systems were piloted by Compass HyStar 3.2 (Bruker). Peak lists were created using DataAnalysis 4.1 (Bruker) and saved as MGF file for use with ProteinScape 3.1 (Bruker) with Mascot 2.4 as search engine (Matrix Science). Enzyme specificity was set to trypsin, and the maximum number of missed cleavages per peptide was set at one. Carbamidomethylation was allowed as fixed modification, oxidation of methionine and biotinylation (K) were allowed as variable modification. Mass tolerance for monoisotopic peptide window was 7 ppm and MS/MS tolerance window was set to 0.05 Da. The peak lists were searched against the *Trypanosoma* taxonomy from UNIREF 100 (176,332 sequences) and proteins identified in the WT control (without BL) were subtracted from the results. Relative enrichment of proteins found only in the two *TbKIFC1*-BL strains was analyzed in TriTryp database for Gene Ontology (GO) term enrichment.

Production of rAPOL1. Recombinant APOL1 was prepared according to the procedure already described (Vanhamme et al., 2003). The purity and concentration were verified by SDS-PAGE and Coomassie blue staining.

***In vitro* trypanolysis and growth assays.** Lysis assays were performed as in (Pérez-Morga et al., 2005; Vanhamme et al., 2003). Normalizations were performed to untreated controls. For the measurements of SHP1 peptide toxicity, parasites were incubated for 90 min at 37°C with the peptide before counting.

Mice infection. NMRI and C57BL/6 mice, either WT or µMT KO, were used for these experiments. 24 h before mice infection, the *TbKIFC1*^{RNAi} and addback parasites were incubated *in vitro* with 1µg/ml doxycyclin to induce RNAi, and mice were given 1 mg/ml doxycyclin with 5g/L sucrose in drinking water (Lecordier et al., 2005). For infection, parasites were concentrated to inject intraperitoneally 10^5 cells in 100 µl per mouse. Drinking water was replaced the day of infection and every two days during the course of infection. Parasitaemia was monitored by tail blood puncture. WT and µMT KO C57BL/6 mice were infected under the same conditions. Sample size was empirically estimated and validated by the stability of the standard deviation of the growth curves. Within each experiment, animals used were morphologically undistinguishable (same strain, age and weight) and allocated randomly to each group. No blinding was done. For experiments aiming at evaluating the effects of phagocytic cells, mice were injected 3 days before infection with 200µl of liposomes containing either phosphate buffered saline (PBS) or clodronate (Liposoma Research).

Antibodies. Rabbit immune serum and purified anti- MITat 1.1 VSG antibodies (IgMs and IgGs) were generated as previously described (O'Beirne et al., 1998). Normal mouse serum was obtained from healthy mice after clotting for 1 h at 37°C.

Aggregation assay. This assay was performed essentially as in O'Beirne et al., (1998). Monomorphic MITat 1.1 bloodstream forms were incubated at 37 °C (5% CO_2) at 1 x 10^7 cells/ml in HMI9 containing 10% fetal calf serum. After preincubation for 10 min, purified anti-VSG IgG or IgM was added. Samples (10 µl) were removed at various times (see Figs. 4, S3, S4) and diluted in 90 µl of ice-cold PSG [3 mM NaH_2PO_4, 57 mM Na_2HPO_4, 44 mM

NaCl, 5 mM KCl, 1 mM $MgCl_2$, 10 mM glucose and 70 mM sucrose (pH 8.0)] and the numbers of free non-aggregated cells were counted in duplicate immediately. The percentage of aggregated cells was determined (O'Beirne et al., 1998).

Analysis of clearance of surface bound antibodies by flow cytometry. The clearance of surface bound anti-VSG antibodies from individual cells was also monitored by flow cytometry. Cultures of exponentially growing MITat 1.1bloodstream forms were collected by centrifugation for 5 min at 1500 g, and resuspended (10^7 cells/ml) in ice-cold HMI9 + fetal calf serum. The suspension of cells (5 ml) was incubated on ice with rabbit immune serum (1:1000 dilution) for 1 h and then transferred to 10 ml of ice-cold HMI9 + fetal calf serum, and centrifuged for 5 min at 1500 g (4 °C). The supernatants were removed and the pellets were quickly resuspended in 5 ml of pre-warmed (37 °C) HMI9 medium. A sample (500 µl) was removed immediately and transferred to an equal volume cold fixation solution (6% PFA in PBS, pH 7.5) in a 15 ml centrifuge tube and kept on ice. At various times additional samples (see Figs. 4 and S5) were removed and transferred to fixation solution as above. After 15 min fixation 14 ml of cold quench solution (PBS + 2 mM glycine) were added and the cells were centrifuged for 5 min at 1500 g (4 °C), washed once in PBS and resuspended in 250 µl (~ 2 x 10^7 cells/ml) in cold PBS. Samples (0.1 ml) of fixed cells were incubated for 1 h at 4 °C with an equal volume of Alexa-488 labelled goat anti-rabbit IgG diluted 1/800 in PBS containing 1% fetal calf serum and 1% BSA. The cells were centrifuged for 30 s at 10,000 g and resuspended in 200 µl of PBS before analysis for Alexa-488 fluorescence by flow cytometry. Flow cytometry was performed on the Accuri C6 flow cytometer (BD; San Jose, USA); AlexaFluor488 fluorescence was detected through the 488 nm laser-533/30 nm filter set.

Analysis of the internalization of surface biotinylated proteins. Endocytosis of surface proteins was monitored using a previously described surface biotinylation assay (Engstler et al., 2004). Cultures of MITat 1.1 cells (0.5-1 x 10^6 cells/ml) were chilled on ice and collected by centrifugation for 5 min at 1500 g (4 °C), and resuspended in ice-cold PSG. Biotinylation was performed on ice by incubating the cells (10^8/ml) with EZ-Link Sulfo-NHS-SS-Biotin (1.6 mM) for 10 min. The cells were transferred to 19 volumes of ice-cold PSG supplemented with 10 mM Tris (pH 8) and centrifuged for 5 min at 1500 g (4 °C), washed and resuspended in PSG (10^8 cells/ml) and transferred to 9 volumes of pre-warmed HMI9 +10% fetal calf serum, and incubated at 37 °C. At various times (see Fig. 4), 500 µl samples were removed and transferred to 19 volumes of ice-cold PSG + 1% BSA, centrifuged for 5 min at 1500 g (4 °C), washed and resuspended in PSG (10^7 cells/ml). An equal volume of stripping buffer [PSG + 10% fetal calf serum and 50 mM reduced glutathione (pH 8.5)] was added and the cells were incubated on ice for 15 min. Ten volumes of ice-cold PSG were added and the cells were collected by centrifugation as before and washed with cold PSG, resuspended in PSG at 5 x 10^7 cells/ml and fixed by the addition of an equal volume cold fixation solution (6% PFA in PBS, pH 7.5) in a 15 ml centrifuge tube and kept on ice. After 15 min fixation 14 ml of cold quench solution (PBS + 2 mM glycine) were added and the cells were centrifuged for 5 min at 1500 g (4 °C), washed once in PBS and resuspended in 250 µl (~ 2 x 10^7 cells/ml) in cold PBS. Samples (0.1 ml) of fixed cells were incubated for 1 h at 4 °C with an equal volume of 40 µg/ml phycoerythrin (PE)-labelled streptavidin in PBS containing 1% BSA and 0.25% Triton X-100. The cells were centrifuged for 30 s at 10,000 g and resuspended in 200 µl of PBS before analysis by flow cytometry. PE fluorescence was detected using the 488 nm laser 585/40 nm filter set.

Return of biotinylated proteins to the surface. Surface-biotinylated bloodstream form cells (as above) were transferred to 9 volumes of pre-warmed HMI9 + 10% fetal calf serum and incubated at 37 °C for 15 min. The cell suspension was then transferred to 19 volumes of ice-cold PSG, centrifuged for 5 min at 1500 g (4 °C), washed and resuspended in PSG (10^7 cells/ml). An equal volume of stripping buffer (ice-cold PSG + 10% fetal calf serum), glutathione was added and the cells were incubated on ice for 15 min. Ten volumes of ice-cold PSG were added and the cells were collected by centrifugation as before and washed with cold PSG. The cells were then resuspended (10^7 cells/ml) in pre-warmed HMI9 + 10% fetal calf serum and incubated at 37 °C. At various times (see Fig. 4), 500 µl samples were removed and added to an equal volume of cold fixation solution (6% PFA in PBS, pH 7.5). After fixation and washing, the cells were resuspended in 250 µl (~ 2 x 10^7 cells/ml) in cold PBS. Surface fluorescence was detected by incubation of fixed cells for 1 h at 4 °C with an equal volume of 40 µg/ml PE-labelled streptavidin in PBS containing 1% BSA. The cells were centrifuged for 30 s at 10,000 g and resuspended in 200 µl of PBS before analysis by flow cytometry. PE fluorescence was detected using the 488 nm laser 585/40 nm filter set.

FRAP analysis. FRAP assays were performed essentially as in Uzureau et al. (2013). Briefly, 2 x 10^6 bloodstream *T. brucei* cells were labelled with 1 µM sulfo-N-hydroxysulfosuccinimide coupled Atto 488 fluorescent dye (ATTO-TEC GmbH, Siegen) for 15 min on ice and washed two times with cold PBS buffer containing 80 mM glucose. In some experiments, WT parasites were preincubated for 30 min at 37°C with 2.5 mM MBCD before labeling. The trypanosomes were immobilized on a 1.25 % low melting point agarose pad sealed with rubber glue. The samples were put in an incubation chamber thermo-stabilized at 30 °C. Under these conditions the parasites remained alive (flagellum beating) for at least 6 h. FRAP analysis was performed with a Zeiss LSM 710 confocal microscope.

For each cell 20 pre-bleach and 80 post-bleach acquisitions were made. The mobile fraction was calculated according to the Zeiss Zen 2010 software using a double normalization (background and reference image).

Mobility assay. MITat 1.1 WT and *TbKIFC1*^{RNAi} parasites were concentrated at 2.5 x 10^6 cells/ml and maintained for 30 min at 37°C with or without anti-MITat 1.1 VSG antibody. The parasites were then loaded in microwells containing solidified Matrigel. Images were acquired for 40 sec at 500 ms interval (Axio Observer Z1). Cell tracking was performed using Fiji software and the MTrackJ module (Meijering et al., 2012).

Phagocytosis assay. Phagocytosis assay of MITat1.1 WT and *TbKIFC1*^{RNAi} trypanosomes was performed with murine RAW264.7 macrophages seeded on coverslips exactly as in Cheung et al. (2016). Parasites were opsonized with 10% normal mouse serum or anti-MITat 1.1 antibodies for 30 min at 37°C before co-incubation with activated macrophages for 90 min. Cells were fixed with 2% PFA and permeabilized in methanol at -20°C for 30 s. Surface-bound and internalized parasites were detected with anti-MITat 1.1 VSG and anti-rabbit Alexa Fluor 594 antibodies. Coverslips were mounted before immunofluorescence analysis. Consecutive fields were acquired and parasites were counted for 500 to 1,000 macrophages in each condition.

SEM analysis. Parasites and macrophages seeded on coverslips were co-incubated as described above and then fixed overnight at 4°C in 2.5% glutaraldehyde, 0.1M cacodylate buffer (pH 7.2), and post-fixed in OsO4 (2%) in the same buffer. After serial dehydration in increasing concentrations of ethanol, samples were dried at critical point and coated with platinum by standard procedures. Observations were made in a Tecnai FEG ESEM QUANTA

200 (FEI) and images capture with a secondary electron detector and processed by SIS iTEM (Olympus) software.

TEM analysis. Cells were fixed for 1 h at room temperature in 2.5% glutaraldehyde in culture medium, and postfixed in 2% OsO4. After serial dehydration in increasing ethanol concentrations, samples were embedded in agar 100 (Agar Scientific Ltd., UK) and left to polymerize for 2 days at 60 °C. Ultrathin sections (50–70-nm thick) were collected in Formvar-carbon- coated copper grids by using a Leica EM UC6 ultramicrotome and stained with uranyl acetate and lead citrate. Observations were made on a Tecnai10 transmission electron microscope (FEI), and images were captured with an Olympus VELETA camera and processed with AnalySIS and Adobe Photoshop softwares.

Atomic force microscopy. *T. brucei* parasites were fixed for in 5 min at 4°C (on ice) in 3.5% HCHO while in culture medium at 37°C. Samples were washed 3 times for 5 min and resuspended in 0.1 M sodium cacodylate buffer (pH 7.4). Cells were then immobilized onto poly-L-lysine-coated glass-bottomed Petri dishes (WillCo). Dishes were first filled with a 0.5 mg/ml poly-L-lysine solution (PLL, Mw ~ 70-150 kDa) in PBS, incubated at 37°C for 30 min, washed with buffer for 3 min and dried in a laminar flow hood for 2 hours at room temperature. Either WT or *TbKIFC1*^{RNAi} parasite suspensions were plated onto the PLL-coated dishes overnight. The dishes were then washed 3 times with PBS to remove non-attached cells. AFM experiments were performed with a Bioscope Resolve AFM (Bruker) operated in PeakForce QNM mode at ~25-30°C in PBS. PeakForce QNM Live Cell probes (Bruker) with spring constants ranging from 0.08 N to 0.1 N/m and a tip radius of curvature of ~65 nm were used for the measurements. Spring constants were calibrated by the manufacturer with a vibrometer (OFV-551, Polytec, Waldbronn) and they were used to

determine the deflection sensitivity using the thermal noise method (Butt and Jaschke, 1995) before each experiment. FD-based multiparametric maps were acquired using a force setpoint of 1 nN while oscillating the AFM cantilever at 1 kHz with peak-to-peak oscillation amplitudes of 1 µm. Images were recorded using a scan rate of 0.2-0.6 Hz and 128 pixels per line. FD-based AFM maps were processed offline using the NanoScope Analysis 1.80 Software (Bruker). To extract the Young's modulus, we analyzed the retraction part of raw force-distance curves to avoid plastic deformation contributions. The best quality of the fit was obtained when by fitting the contact part of the curve with the Hertz model (Schillers et al., 2017)

$$F^{2/3} = \left(\frac{4}{3}\frac{E}{(1-\nu^2)}\sqrt{R}\right)^{2/3}\delta$$

where E is the Young's modulus, δ is the indentation depth, ν is the Poisson ratio, and R is the contact radius. We used a Poisson's ratio value of 0.3. The upper and lower boundaries of the fit region are defined as the percentage difference between the maximum and the minimum force. Therefore, these boundaries define the indentation depth taken into account in the analysis of the FD curves. We used fit ranges of 5-25%, which would mainly correspond to the contribution of the plasma membrane and 30-90%, which would comprise the contribution of the underlying microtubules (Dumitru et al., 2018).

Lipid analysis. Lipids were analyzed as previously described (Amiar et al., 2016; Dubois et al., 2018). Specifically, total lipid spiked with 10 nmol C13:0 fatty acid and PC (C21:0/C21:0) was extracted by chloroform:methanol, 2:1 (v/v) followed by biphasic separation by adding 0.2% KCl. An aliquot of resulted organic phase containing cholesterol was dried and analyzed by gas chromatography-mass spectrometry (Agilent 5977A-7890B) after derivatization of cholesterol to cholesterol-TMS by BSTFA-TMCS, 99:1 (Sigma). Phospholipids were separated by HPTLC with solvent system (hexane/diethylether/formic

acid, 80:20:2, v/v/v). The phospholipid spot was extracted for the quantification of fatty acids by gas chromatography-mass spectrometry (Agilent 5977A-7890B) after methanolysis. Fatty acid methyl esters and cholesterol-TMS were identified by their mass spectrum and retention time, and quantified by calibration curve generated with internal standards. Then cholesterol and phospholipid content was normalized according to the parasite cell numbers and C13:0 or C21:0 internal standard (Avanti Polar Lipids).

***In situ* tagging**. The pPOTv7 plasmid (Dean et al., 2015) was modified to replace the YFP gene by the mCherry coding sequence. For C-terminal tagging of GRASP (Tb927.11.2660), Sec15 (Tb927.11.7120), Sec1 (Tb927.9.1970), β'COP (Tb927.2.6050), FAZ1 (Tb927.4.3740), and N-terminal tagging of Rab11 (Tb927.8.4330), PCR primers described in TrypTag were used. PCR products were transfected by standard methods in the WT and *TbKIFC1*^{RNAi} cell lines. Parasites were selected with 5µg/ml blasticidin. For double tagging, the β'COP-mCherry tagged strains were transfected with a PCR product for YFP tagging of GRASP obtained from a version of pPOTv7 in which the blasticidin resistance gene had been replaced by the puromycin resistance gene.

Top Fluor cholesterol localization. Parasites were washed in HMI9 medium without serum and resuspended in HMI9 supplemented with 1% FCS and 5 µM Top Fluor cholesterol (Avanti Polar Lipids). Parasites were incubated for 50 min at 37°C before addition of Hoechst and a further 10 min incubation. Parasites were cooled down on ice, washed twice with cold HMI9 medium and resuspended in 10 µl before loading on agarose pads freshly prepared with HMI9 containing 10% FCS and 1.25% low melting point agarose. Cells were imaged immediately with Zeiss LSM 710 confocal or Axioimager M2 epifluorescence microscope with same parameters for all experiments. Fluorescence signals were analyzed with Fiji

software. To measure the intensity of the cholesterol signal within specific organelles, the mean fluorescence intensity of Top Fluor was measured within ROIs (regions of interest) that were delineated using thresholding of the mCherry signal corresponding to the different markers and after background subtraction. In addition, cholesterol enrichment in the membrane structure associated with FAZ was quantified by measuring the fluorescence intensity along a 2 pixels width line manually drawn based on the morphology of the Top Fluor signal. In order to control for variability in fluorescence signal, this quantification was done in all individual cells for each cell line and condition.

Cholesterol depletion. Depletion of cholesterol with methyl-β-cyclodextrin was obtained by a previous incubation of parasites at 37°C for 30 min and a wash with HMI9 medium. 10^5 cells were analyzed by flow cytometry (BD FACS Canto II).

Statistical analysis. Statistical analysis was performed using Prism software (GraphPad). Immunofluorescence data were obtained from randomly selected cells from three independent experiments, and the images shown are representative of the majority of cells. Quantitative data were represented as means ± standard deviation (SD); no sample was excluded. Normality of the data was analysed with the Shapiro-Wilk test. p-values were calculated by the Student's t test and one-way ANOVA (post hoc Dunnett's test) for multiple and single comparisons of normally distributed data respectively, and by the Mann-Whitney test for multiple comparisons of non-normally distributed data (*P < 0.05; **P < 0.01; ***P < 0.001; ****P <0.0001).

Supplemental References

Amiar, S., MacRae, J.I., Callahan, D.L., Dubois, D., van Dooren, G.G., Shears, M.J., Cesbron-Delauw, M.F., Maréchal, E., McConville, M.J., McFadden, G.I., et al. (2016) Apicoplast-localized lysophosphatidic acid precursor assembly is required for bulk phospholipid synthesis in *Toxoplasma gondii* and relies on an algal/plant-like glycerol 3-phosphate acyltransferase. PLoS Pathog. *12*, e1005765.

Berendsen, H. J. C., Postma, J. P. M., van Gunsteren, W. F., DiNola, A., and Haak, J. R. (1984) Molecular dynamics with coupling to an external bath. J. Chem. Phys. *81*, 3684.

Bussi, G., Donadio, D., and Parrinello, M. (2007) Canonical sampling through velocity rescaling. J. Chem. Phys. *126*, 014101.

Butt, H. J., and Jaschke, M. (1995) Calculation of thermal noise in atomic force microscopy. Nanotechnology *6*, 1.

Dean, S., Sunter, J., Wheeler, R.J., Hodkinson, I., Gluenz, E., and Gull, K. (2015) A toolkit enabling efficient, scalable and reproducible gene tagging in trypanosomatids. Open Biol. *5*, 140197.

De Jong, D. H., Singh, G., Bennett, W.F., Arnarez, C., Wassenaar, T.A., Schäfer, L.V., Periole, X., Tieleman, D.P., and Marrink, S.J. (2013) Improved Parameters for the Martini Coarse-Grained Protein Force Field. J. Chem. Theory Comput. *9*, 687–697.

Deleu, M., Crowet, J.M., Nasir, M.N., and Lins, L. (2014) Complementary biophysical tools to investigate lipid specificity in the interaction between bioactive molecules and the plasma membrane: A review. Biochim. Biophys. Acta *1838*, 3171-3190.

Dubois, D., Fernandes, S., Amiar, S., Dass, S., Katris, N.J., Botté, C.Y., and Yamaryo-Botté, Y. (2018) *Toxoplasma gondii* acetyl-CoA synthetase is involved in fatty acid elongation (of long fatty acid chains) during tachyzoite life stages. J. Lipid Res. *59*, 994-1004.

Dumitru, A. C., Poncin, M.A., Conrard, L., Dufrêne, Y.F., Tyteca, D., and Alsteens, D. (2018) Nanoscale membrane architecture of healthy and pathological red blood cells. Nanoscale Horizons *3*, 293-304.

Essmann, U., Perera, L., Berkowitz, M.L., Darden, T., Lee, H., and Pedersen, L.G. (1995) A smooth particle mesh Ewald method. J. Chem. Phys. *103*, 8577.

Hermans, J., Berendsen, H.J.C., Van Gunsteren, W.F., and Postma, J.P.M. (1984) A consistent empirical potential for water-protein interactions. Biopolymers *23*, 1513–1518.

Hess, B., Bekker, H., Berendsen, H.J.C., and Fraaije, J.G.E.M. (1997) LINCS: A linear constraint solver for molecular simulations. J. Comput. Chem. *18*, 1463–1472.

Hess, B., Kutzner, C., van der Spoel, D., and Lindahl, E. (2008) GROMACS 4: algorithms for highly efficient, load-balanced, and scalable molecular simulation. J. Chem. Theory Comput. *4*, 435–447.

Humphrey, W., Dalke, A., and Schulten, K. (1996) VMD: visual molecular dynamics. J. Mol. Graph. *14*, 33–38.

Ingólfsson, H.I., Melo, M.N., van Eerden, F.J., Arnarez, C., Lopez, C.A., Wassenaar, T.A., Periole, X., de Vries, A.H., Tieleman, D.P., and Marrink, S.J. (2014) Lipid organization of the plasma membrane. J. Am. Chem. Soc. *136*, 14554–14559.

Krieg, M., Fläschner, G., Alsteens, D., Gaub, B.M., Roos, W.H., Wuite, G.J.L., Gaub, H.E., Gerber, C., Dufrêne, Y. F., and Müller, D.J. (2019) Atomic force microscopy-based mechanobiology. Nat. Rev. Physics *1*, 41–57.

Lecordier, L., Walgraffe, D., Devaux, S., Poelvoorde, P., Pays, E., and Vanhamme, L. (2005) *Trypanosoma brucei* RNA interference in the mammalian host. Mol. Biochem. Parasitol. *140*, 127-131.

Lins, L., Thomas-Soumarmon, A., Pillot, T., Vandekerckhove, J., Rosseneu, M., and Brasseur, R. (1999) Molecular determinants of the interaction between the c-terminal domain of Alzheimer's β-amyloid peptide and apolipoprotein E α-helices, J. Neurochem. *73*, 758–769.

Marrink, S.J., Risselada, H.J., Yefimov, S., Tieleman, D.P., and de Vries, A.H. (2007) The MARTINI force field: coarse grained model for biomolecular simulations. J. Phys. Chem. B *111*, 7812–7824.

Meijering, E., Dzyubachyk, O., and Smal, I. (2012) Methods for cell and particle tracking. Methods in Enzymology *504*, 183-200.

Monticelli, L., Kandasamy, S.K., Periole, X., Larson, R.G., Tieleman, D.P., and Marrink, S. (2008) The MARTINI coarse-grained force field: extension to proteins. J. Chem. Theory Comput. *4*, 819–834.

Poon, S.K., Peacock, L., Gibson, W., Gull, K., and Kelly, S. (2012) A modular and optimized single marker system for generating *Trypanosoma brucei* cell lines expressing T7 RNA polymerase and the tetracycline repressor. Open Biol. *2*, 110037.

Schillers, H., Rianna, C., Schäpe, J., Luque, T., Doschke, H., Wälte, M., Uriarte, J.J., Campillo, N., Michanetzis, G.P.A., Bobrowska, J., et al. (2017) Standardized nanomechanical atomic force microscopy procedure (SNAP) for measuring soft and biological samples. Scient. Reports *7*, 5117.

Schmid, N., Eichenberger, A.P., Choutko, A., Riniker, S., Winger, M., Mark, A.E., and van Gunsteren, W.F. (2011**)** Definition and testing of the GROMOS force-field versions 54A7 and 54B7. Eur. Biophys. J. *40*, 843–856.

Schrödinger, L. (2010) The PyMOL molecular graphics system, version 1.3.

Wassenaar, T.A., Pluhackova, K., Böckmann, R.A., Marrink, S.J., and Tieleman, D.P. (2014**)** Going backward: a flexible geometric approach to reverse transformation from coarse grained to atomistic models. J. Chem. Theory Comput.*10*, 676-690.